The DOI for this manuscript is doi: 10.1175/MWR-D-17-0121.1

Elevated Mixed Layers and Associated Severe Thunderstorm Environments in South and North America

BRUNO Z. RIBEIRO*

Centro de Previsão de Tempo e Estudos Climáticos, Instituto Nacional de Pesquisas Espaciais (CPTEC/INPE), Cachoeira Paulista, São Paulo, Brazil

LANCE F. BOSART

Department of Atmospheric and Environmental Sciences, University at Albany, State University of New York, Albany, New York

* Corresponding author e-mail: bruno.ribeiro@cptec.inpe.br

ABSTRACT

This study presents a climatological and composite analysis of elevated mixed layers (EMLs) in South and North America derived from the NCEP Climate Forecast System Reanalysis. The EMLs are identified based on objective criteria applied to the reanalysis data. Composite analyses of synoptic-scale conditions and severe weather parameters associated with spring EML cases are presented. EMLs are more frequent immediately to the east of the Andes and the Rockies. The North American EMLs form by surface heating over the higher terrain of the Rockies, with peak frequency occurring in spring and summer. EMLs in South America are generated by differential temperature advection due to ageostrophic circulations east of the Andes, as indicated by the

temperature lapse rate tendency equation, which relates to the higher frequency of EMLs during the cold season in South America. EMLs over North America are about 100 hPa lower than over South America due to the lower height of the Rockies in comparison to the Andes.

The synoptic conditions associated with EMLs in South and North America are characterized by an upper-level trough upstream and low-level moisture flux convergence due to poleward-directed flow, favoring synoptic-scale ascent poleward of the EML location, where the convective inhibition is relatively low. When EMLs occur, higher surface-based convective available potential energy and low-level storm-relative helicity in association with lower lifting condensation level heights observed in North America indicate that surface-based supercell storms and tornadoes are more likely in this continent in comparison with South America, corroborating observations.

1. Introduction

Elevated Mixed Layers (EMLs) are layers of constant vertical distribution of potential temperature (θ), i.e., layers having dry-adiabatic temperature lapse rates, not coupled to the ground (Carlson and Ludlam 1968; Lanicci and Warner 1991a, hereafter LW91). These layers occur mainly to the east (downstream) of great mountain ranges, a result of horizontal advection of surface-heated air over higher terrain and/or ageostrophic circulations in the lee of the mountains. The Rockies in North America (NA; e.g., Carlson and Ludlam 1968; Banacos and Ekster 2010, hereafter BE10) and the

Tibetan Plateau in east Asia (e.g., Das et al. 2014) are known to favor the formation of EMLs that can have a great impact on the atmospheric conditions over the lower terrain downstream due to their association with hazardous weather events (Cordeira et al. 2017). Observations and case studies by Rasmussen and Houze (2016) show EMLs occur east of the Andes in South America (SA). The purpose of this paper is to document SA EMLs and to compare and contrast their formation processes with NA EMLs.

A complete climatology of NA EMLs was done by Lanicci and Warner (1991a,b,c) in three sequential papers (here we will refer to the "Part 1" paper as LW91). They used observed NA soundings from 1983 to 1986, and applied several criteria to automatically search for EMLs. The classic model of EML formation depicts an approaching trough in the middle and upper troposphere and associated southwesterly flow over the high terrain in northern Mexico/southwestern United States (U.S.). This southwesterly flow advects a dry, mixed air mass from over higher terrain eastward over somewhat less warm but much more moist planetary boundary layer (PBL) air at lower elevations over the Great Plains. This setup can create an environment of high potential instability over the Great Plains, and is often observed from spring to summer, when solar radiation is strong enough to form deep, surface-based mixed PBLs over the Rockies.

The mechanisms for EML formation and maintenance in NA were investigated by BE10. The authors presented an equation for the local tendency of temperature lapse rate (γ; $\gamma \equiv -dT/dz$, where T is temperature and z is height). The local γ tendency is given by

$$\frac{\partial \gamma}{\partial t} = \underbrace{-\frac{1}{c_p}\frac{\partial Q}{\partial z}}_{A} \underbrace{-\mathbf{V}\cdot\boldsymbol{\nabla}_{\mathrm{h}}\gamma}_{B} \underbrace{-w\frac{\partial \gamma}{\partial z}}_{C} + \underbrace{\frac{\partial \mathbf{V}}{\partial z}\cdot\boldsymbol{\nabla}_{\mathrm{h}}T}_{D} + \underbrace{\frac{\partial w}{\partial z}(\Gamma_d - \gamma)}_{E}, \qquad (1)$$

where Q is the diabatic heating rate, $\mathbf{V}$ is the horizontal wind vector, w is the vertical velocity, c_p is the specific heat of dry air at constant pressure and Γ_d is the dry-adiabatic temperature lapse rate. Term A is the differential diabatic heating rate; terms B and C are the horizontal and vertical γ advection, respectively; term D is the differential horizontal temperature advection (associated with the ageostrophic wind, since the differential horizontal temperature advection by the geostrophic wind is zero); and term E is the stretching term. The scale analysis performed by BE10 showed that the horizontal advection of γ is 1–2 orders of magnitude greater than the other terms, and corroborates previous studies of EMLs in NA (Carlson and Ludlam 1968; LW91). This equation will be used to analyze the physical processes associated with EMLs east of the Andes and Rockies, respectively.

Severe thunderstorms occur in thermodynamically unstable environments where the vertical wind shear is high, and there is sufficient lifting capable to trigger convection and release the thermodynamic instability (Thompson et al. 2003; Brooks et al. 2003). In this context, EMLs are well known to be associated with severe thunderstorms (e.g., Carlson and Ludlam 1968; LW91; Lanicci and Warner 1991c; BE10, Cordeira et al. 2017). The concomitant occurrence of moderate convective inhibition (CIN) caused by the temperature inversion in the base of the EML, high convective available potential energy (CAPE) associated with steep γ in the EML over a warm/moist PBL, and sufficient vertical wind shear, are recognized to favor severe thunderstorms in NA.

Despite being an important feature, the EML is not a sufficient ingredient for severe thunderstorm formation (Cordeira et al. 2017), and can prevent convective initiation in some cases (Carlson and Ludlam 1968). In SA, the EMLs influences on severe thunderstorm environments are likely similar to NA.

Brooks et al. (2003) have shown that southeastern SA, despite being a hot spot for severe thunderstorms in the world (Velasco and Fritsch 1987; Zipser et al. 2006), has a lower frequency of “tornado environments” than NA. Both Americas have a vast amount of land east of the mountain ranges, but there are several geographical characteristics that contribute to their different severe thunderstorm climatologies. One of the main differences is the moisture source: the Gulf of Mexico in NA as compared to the Amazon Basin in SA. The Amazon is dry in the cold season of Southern Hemisphere, whereas the Gulf of Mexico remains warm, and consequently moist, throughout the cold season in Northern Hemisphere. Agricultural lands can also contribute to the moisture budget through evapotranspiration processes. Another important feature is the shape of the mountain ranges: both have north-south orientation in the subtropical and extratropical latitudes, but in general the Rockies are longitudinally wider, whereas the Andes are higher and have steeper slopes (Fig. 1). The Andes form a higher barrier to the low to mid tropospheric flow while the broader Rockies act as an elevated heat source, mainly in the warm season, because of their flatter shape. All of these characteristics likely influence severe thunderstorm environments to the east of the mountains.

In this paper, an objective methodology to identify EMLs was used to build a climatology of EMLs in SA and NA. The characteristics of EMLs in both continents and the synoptic environments related to their occurrence were analyzed. The scientific questions that arise in this research are: How often and where do EMLs occur in SA east of the Andes? How do the EML climatologies over SA and NA compare? What are the differences in characteristics of the EMLs, such as thickness and base height? What is the influence of EMLs in the severe weather environments in SA that might explain the meteorological differences between both continents? This study is the first to quantify EML occurrence east of the Andes and the associated synoptic-scale environments, addressing the above questions. It is currently unknown what the characteristics of SA EMLs are and their potential influence on observed convection in SA, and whether or not any similarities can be drawn with NA EMLs.

The paper is organized as follows: Section 2 presents data and methodology; Section 3 shows the results, divided into characteristics of EMLs in both continents (Section 3.1) and the composites of EML cases over the regions (Section 3.2), along with discussions of the main findings; and, in Section 4, a synthesis of the paper results is shown and the conclusions are discussed.

2. Data and Methodology

This study was focused on midlatitudes and subtropical latitudes of NA and SA, east of the Rockies and Andes, respectively. The NA study area is bounded by 20°N to 50°N and 110°W to 80°W; the SA study area is bounded by 13°S to 43°S and 72°W to 42°W (Fig. 1).

2.1. Dataset

The main analyses in this paper were constructed using the NCEP Climate Forecast System Reanalysis (CFSR; Saha et al. 2010), which has a native horizontal resolution of T382 (~38 km, interpolated to a horizontal grid spacing of 0.5°x0.5°) and is available at synoptic hours (0000, 0600, 1200, 1800 UTC). Since the CFSR is a global reanalysis, it allows a direct comparison between NA and SA by applying the same analysis methods in both continents. Observed soundings from the University of Wyoming webpage (http://weather.uwyo.edu/upperair/sounding.html) were also used to validate the methodology.

The observed soundings network in SA has only a few observations near the Andes in Paraguay, northern Argentina, and Bolivia (Fig. 1). The lack of soundings in this area results in a deficient representation of meteorological phenomena east of the Andes. As a result, the intensity of the low-level jet in numerical models is underestimated (Salio et al. 2007). The majority of SA soundings are available only after 2000, and several periods in the time series had either no soundings, or soundings only at one synoptic time (e.g., 0000 UTC). We chose the CFSR for this research because of the low number of soundings in SA east of the Andes and the lack of continuity in their time series.

Four examples of typical EMLs in observed and CFSR soundings are shown in Fig. 2, two in SA (Figs. 2a,b) and two in NA (Figs. 2c,d). Little differences are observed in the wind and temperature profiles, but the dewpoint temperature profiles present large discrepancies in some layers. Other research found the same difficulty of reanalysis datasets to correctly represent the moisture profiles (e.g., Bao and Zhang 2013; Chen et al. 2014). The more pronounced differences in the temperature profile are found near the EML base, and are associated with the coarser vertical resolution of the CFSR. The nearly dry-adiabatic γ within the EML is well represented by the CFSR.

We performed a comparison of 6214 observed soundings with CFSR soundings. Both observed and CFSR soundings had to exhibit EMLs. The EMLs were identified using the methodology presented in the next subsection. Table 1 presents the differences in EML characteristics between observed and CFSR soundings. There is no statistically significant (95% confidence using the Student's t-test) difference between EML bases in observed and CFSR soundings. The EML thickness, however, is greater in CFSR soundings by nearly 15 hPa. The EML γ is lower (average difference of 0.68 K km^{-1}) and the EML θ is higher (average difference of 0.55 K) in CFSR soundings. The differences between SA observed and CFSR soundings are also greater than NA soundings for most of the parameters, which is likely due to the lower number of observations in SA that leads to relatively lower quality of the reanalysis. The differences between observed and CFSR soundings are related to numerous factors, such as data assimilation and coarser vertical resolution of the reanalysis. However, the errors are sufficiently small to allow climatological studies using reanalysis (Brooks et al. 2003), and the reanalysis provide a better areal/temporal coverage than observed soundings.

2.2. Definition of Elevated Mixed Layer

We define an EML as a layer having a γ of at least 7.5 K km^{-1} and thickness of at least 150 hPa, with its base higher than 1000 m above ground level. The base is considered the first pressure level, from bottom to top, to have γ greater or equal to 7.5 K km^{-1}. This γ threshold is lower than that used in other research [BE10 and Cordeira et al. (2017) used 8.0 K km^{-1}] because the CFSR has less steep γ in the EML than observed soundings (Table 1). An analysis of different thresholds was conducted, and a γ of 7.5 K km^{-1} in the CFSR soundings was in good agreement with EMLs in observed soundings (Fig. 2). A threshold of 150 hPa for EML thickness was used by Cordeira et al. (2017), and is less restrictive than the other thresholds tested (between 150 and 250 hPa). The mean EML thicknesses, shown in Sec. 3.1, are generally greater than 200 hPa, so 150 hPa is a suitable EML thickness threshold. Also, the relative humidity at the top of the EML must be higher than at the base, as in BE10.

The term "EML" is used to refer to a layer that has been mixed through surface radiative warming over higher terrain and advected over lower terrain (e.g., LW91, BE10). Even though elevated layers with steep γ in SA may be formed by other physical processes, in this paper we use the term "EML" to refer to these layers as well. Several authors (e.g., LW91; Cordeira et al. 2017) also refer to layers with steep γ as EMLs without discriminating the physical processes responsible for their formation. Mechanisms other than horizontal advection can play an important role in increasing the γ in NA as well (BE10).

Since one of the main foci of this research is the association of EMLs with severe thunderstorm environments, we require that EML gridpoints must have at least 100 J kg^{-1} of most unstable CAPE (MUCAPE). This threshold prevents EMLs generated by dynamically forced subsidence behind upper-level troughs from being identified (J. M. Cordeira, personal communication). We also tested this threshold by comparing the CFSR EML soundings with the observed EML soundings after upper-level trough passage. The sensitivity tests showed that EMLs behind upper-level trough are generally associated with zero MUCAPE because the low-level air is relatively cold. The composites shown in Section 3 corroborate the efficiency of this methodology in eliminating these cases.

Our automated algorithm proceeds as follows: 1) verify if a gridpoint has MUCAPE of at least 100 J kg^{-1}; 2) if so, look for a pressure level, from bottom to top, with γ of at least 7.5 K km^{-1}; 3) verify if this γ threshold is continuously observed in other levels above, reaching at least 150 hPa in thickness; 4) verify if RH in the first level (EML base) is lower than in the last level (EML top) with the lapse-rate threshold. If these sequential criteria are met, an EML is attributed to that gridpoint at that synoptic time. The algorithm also verifies if the γ below the EML base is higher than 7.5 K km^{-1}. If so, the EML is not accounted, since it is in fact a surface-based mixed layer. Since γ tends to Γ_d in the upper troposphere, upper-level dry-adiabatic layers are discarded by limiting the EML bases to the 500-hPa level. This test is done for every gridpoint in the study areas (Fig. 1) in the 32 years of the CFSR. For every identified EML, the base level, thickness, mean γ and mean θ is accounted.

2.3. Synoptic-scale composite analyses

CFSR-based composite analyses were generated over three 5°x5° regions for synoptic times with EMLs in both continents. Two regions were located close to the mountains at different latitudes [region 1 (R1) in lower latitudes and region 2 (R2) in higher latitudes]. A third region (R3) was chosen between R1 and R2 but was located farther east (Fig. 1). All three regions are located within the 4% EML frequency contour (Fig. 3). Composite analyses in R1 and R2 illustrate synoptic flow configurations associated with EMLs in the frequency maximum region (R1) and poleward-shifted EMLs (R2), respectively. Composite analyses in R3 location illustrate the synoptic flow configurations of EMLs that have transported downstream from their origin. Hereafter, we will use the term “region” to refer to the 5°x5° area, where the EML is located in the composites.

If an EML was identified in at least 80% of the gridpoints within these 5°x5° areas (97 of 121 gridpoints), this synoptic time was considered to have an EML over the region. Several other percentages between 70 and 100% were tested by comparing observations with the identification method, and 80% was used in this research. Values higher than 80% are too restrictive, i.e., the number of EML cases decreases significantly by using higher percentages, which is attributed to the typical heterogeneity in areal coverage of the EMLs. A percentage of 100% was rarely observed. Values lower than 80% were associated with a higher number of cases, but no change in the general synoptic pattern.

The diurnal cycle is not considered in the composites. Even though EML formation in NA relates to the diurnal cycle (Carlson and Ludlam 1968; LW91), the same may not be true in SA. Therefore, the composited cases mix EMLs occurring at any time of the day to allow a comparison between the continents. The composite fields were also used to estimate the γ tendency equation terms [(1); BE10]. All the variables in the equation are directly available in CFSR. Only R1 composites were used for the γ tendency equation computation, since R1 has the highest frequency of EMLs.

Several parameters commonly used in severe thunderstorm forecasting and research were composited. The parameters are: surface-based CAPE (SBCAPE), MUCAPE, CIN of the most unstable parcel (hereafter only "CIN"), lifting condensation level (LCL) height, storm-relative helicity (SRH), and vertical wind difference (hereafter referred only as "wind shear"). These severe weather parameters were averaged in the 5ºx5º areas at synoptic times with EMLs over the regions to compare their variability between the regions and continents. The LCL height was calculated with the Espy formula (Lawrence 2005). The storm motion vector for SRH calculation was estimated using the technique presented by Davies and Johns (1993). The Student's t-test was used to verify if the differences in severe weather parameters between different regions are statistically significant.

Three-month seasons were used to define EML characteristics and to construct the composite analyses. Here "spring," for example, refers to March, April and May in NA and to September, October and November and so on. Although EML composite analyses were constructed for all four seasons, in this paper we will only focus spring cases when the Americas are most frequently affected by severe weather (e.g., LW91; Brooks et al. 2003; Thompson et al. 2003) and when more EML cases were observed.

3. Results and discussion

3.1. Climatology and EML characteristics

Figure 3 shows the percentage of CFSR times that an EML was present in each gridpoint for the four seasons. EMLs are more common east of the mountain ranges in both continents. EML frequencies in SA (Figs. 3a–d) have a nearly constant maximum that varies in location throughout the year. The highest EML frequencies move from northeastern Argentina in winter (Fig. 3d) to east-central Argentina in summer (Fig. 3b), when the areal coverage is the lowest. Higher frequencies extend farther east from fall to spring (Figs. 3a–d), when upper-tropospheric winds are stronger, but are restricted to the Andes foothills in summer (Fig. 3b). Figures 3a–d also indicates that there are only a few sounding sites in north/northwestern Argentina, where most EMLs occur.

Seasonal EML variability in NA is higher with the highest frequency observed in spring (Fig. 3e) over the south-central U.S. and northeastern Mexico, extending north towards the central U.S. This maximum shifts poleward to the north-central U.S. in summer with a reduced magnitude (Fig. 3f). During fall and winter (Figs. 3g,h), fewer EMLs are observed in NA, and most of them occur near the Gulf of Mexico. The NA

EML frequencies during spring are very similar to the findings of LW91 (their Fig. 5). The highest frequencies in the south-central U.S. are related to heating over high terrain in northern Mexico. From late spring to summer, heating is also strong over the high terrain in the western U.S., which favors higher frequencies farther north in the central and north/central U.S. (Fig. 3f). Lower solar elevation angles, snow cover over the Rockies and lower CAPE over NA during fall and winter are consistent with lower EML frequencies during these seasons (Figs. 3g,h).

The EML bases over SA are generally located between 600 and 650 hPa (Figs. 4a–d). These bases are higher (550–600 hPa) during fall (Fig. 4c) and lower (700–650 hPa) in some parts of the study area during summer and spring (Figs. 4a,b). EML thicknesses decrease eastward in all seasons. The greatest EML thicknesses occur in western Argentina during winter (Fig 4d) while shallower EMLs occur in summer (Fig 4b). The occurrence of thicker EMLs during spring and winter (Figs. 4a,d) is associated with a stronger 250-hPa jet in these seasons (Figs. 3a,d).

The main difference of EMLs in NA compared to SA is on their base heights (Fig. 4). The heights vary from 700 to 750 hPa in the areas east of the Rockies during spring and summer (Figs. 4e,f), and are approximately 100 hPa lower than in SA east of the Andes. SA EML thicknesses are maximized in winter in western Argentina (Fig. 4d), when the winds aloft are the strongest, whereas over NA the EMLs have little variation in the thickness maximum (Fig. 4e,f). NA EML thicknesses present a northward shift from spring to summer, with decreasing thicknesses over south-central U.S. and increasing thicknesses over the north-central U.S. (Figs. 4e,f). This northward shift is a result of deeper PBL mixing over higher terrain occurring farther north in summer (LW91).

The highest mean EML γ are found close to the mountain ranges in both continents (Fig. 5). The highest γ in SA occur in winter (Fig. 5d), exceeding 8.0 K km^{-1} in northern Argentina. EMLs in SA also present the lowest γ in summer (Fig. 5b). In NA, the highest γ occur in spring in the central U.S. (more than 8.1 K km^{-1}; Fig. 5e), and farther north in summer (Fig. 5f), following the northward shift in EML frequencies (Figs. 3e,f). During spring and summer, when severe thunderstorms are more common, the γ associated with EMLs over NA is higher than over SA in general (Figs. 5a,b,e,f).

The mean θ in the EML (hereafter "EML θ") is higher in SA in all seasons (Fig. 5) as compared to NA. This result is expected, since EML bases in SA are higher and θ usually increases with height in the troposphere. In spring, SA EML θ distribution (Fig. 5a) is characterized by higher values over northern Paraguay and southern Bolivia, decreasing southward to central Argentina, where the isentropes are nearly zonal. The meridional gradient of EML θ in west-central Argentina persists in the other seasons (Figs. 5b–d). Unlike SA, NA EML θ values are quasi constant in spring and summer (Figs. 5e,f), likely a result of the homogeneous horizontal advection of surface-based mixed layers (BE10). The EML θ values between 316 and 320 K in NA are in good agreement with the findings of LW91 (their Fig. 10).

3.2. Composites and γ tendency equation

3.2.1. Synoptic-scale environment

Standardized 250-hPa geopotential height anomalies (Fig. 6) exhibit a similar large-scale pattern in all composites, with an anomalous trough over the mountain ranges and an anomalous ridge downstream. In SA, the ridge and trough anomalies positions are similar in R1 and R3 composites (Figs. 6a,c), but the ridge is stronger and closer to the EML location in R2 composites (Fig. 6b). The 250-hPa wind magnitude has two maxima, one located over the Andes around 30°S and other extending from eastern Argentina to the Atlantic Ocean at nearly 40°S. The EML region is located in the equatorward entrance region of the jet in R1 and R2 composites (Figs. 6a,b), and farther east in R3 composites (Fig. 6c).

A similar 250-hPa pattern is observed in NA composites (Figs. 6d–f). An anomalous trough is located over the Rockies and an anomalous ridge over the central U.S. The position of the anomalous ridge in relation to the anomalous trough varies between the NA composites, occurring at lower latitudes in R1 and R3 (Figs. 6d,f) and same latitude in R2 (Fig. 6e). The jet stream is poleward in R2 composites in comparison to R1 and R3 composites, similarly to SA, which is caused by the greater amplitude of the flow. The upper-level flow amplitude is greater in NA, whereas in SA the trough and ridge are positively tilted and favor stronger zonal winds.

Vertical motion composites (ω; Fig. 7) in the EML (600–400-hPa layer in SA and 700–500-hPa layer in NA) show that ascent occurs over and mainly poleward of the R1–R3 regions. This area of ascent is downstream of the upper-level trough and in the equatorward entrance region of the jet (Fig. 6) where ascent is favored by ageostrophic circulations (Uccellini and Johnson 1979). Subsidence occurs east of the mountain ranges, mainly in SA.

The γ values increase rapidly from west to east of the Andes following the mean flow (Figs. 7a–c), evidence of the role of the mountains in steepening the γ. Over NA, high γ is observed over the plateaus of northern Mexico in R1 and R3 composites (Figs. 7d,f) and western U.S. in R2 composites (Fig. 7e). High γ values in the 700–500-hPa layer over these areas, where the surface pressure is nearly 800–700 hPa, are related to surface-based mixed layers. The similarity between γ in NA R1 and R3 composites (Figs. 7d,f) indicate the EML is advected from northern Mexico in both cases, but the stronger mean winds are responsible to greater eastward displacement of the EML in R3 composite (Fig. 7f). EMLs occurring over NA R2 are advected by the mean flow from the U.S. Rockies. SA R3 composites (Fig. 7c) suggest the EMLs that reach farther east have their γ reduced, whereas over NA the EMLs maintain the high γ along the flow (Fig. 7f). Ascent in association with lower γ, as observed in SA R3 composites, is responsible for greater γ reduction by vertical advection [term C of (1)], as will be shown in the next subsection.

The general pattern at 850 hPa (Fig. 8) is for lower geopotential heights to occur near the mountain ranges with heights increasing eastward toward the subtropical anticyclones, providing a poleward-directed, confluent flow over and mainly poleward of the R1–R3 regions, where the 1000–800-hPa moisture flux convergence (MFC; Banacos and Schultz 2005) maximizes. A meridional θ_e gradient exists poleward of the R1–R3 regions collocated with high MFC in all composites, which relates to warm front activity

(Banacos and Schultz 2005) along the trough extending east from the lee geopotential height minimum.

The highest θ_e values in SA are found east of the Andes around 20°S in all composites (Figs. 8a–c), in association with northerly flow and MFC along the mountains. The strong 850-hPa winds collocated with MFC along the Andes between 20 and 30ºS, particularly in R1 and R2 composites (Figs. 8a,b), indicate the presence of a barrier jet along the Andes foothills. The longer meridional stretch of 850-hPa winds in the R2 composites (Fig. 8b) is due to the farther west location of the south Atlantic subtropical anticyclone in comparison to the other composites, and also reflects the different location of the anomalous 250-hPa ridge in the R2 composites (Fig. 6b). Several climatological studies in SA relate similar low-level conditions to the occurrence of mesoscale convective systems and severe thunderstorms (e.g., Machado et al. 1998, Salio et al. 2007; Anabor et al. 2008), especially in the areas of greatest MFC.

The distribution of 850-hPa θe in the NA composites (Figs. 8d–f) shows maxima in northern Mexico and the southern U.S. Southwesterly flow is observed from the western Gulf of Mexico towards the Great Lakes region. In the R2 composites (Fig. 8e), stronger southerly flow spreads warm/moist air northward along the Rockies, whereas in the R1 and R3 composites (Figs. 8d,f) the greater zonal component of the flow enables high-θ_e air to be confined to lower latitudes. All NA composites exhibit stronger 850-hPa flow over the regions in comparison to SA composites, and a similar pattern of higher MFC poleward of the EML location.

3.2.2. γ tendency equation

Figure 9 shows the quantification of the γ tendency equation terms derived from (1) and calculated using the composite fields of 133 EML cases over SA R1. Term A (Fig. 9a,f) is relatively small over SA and NA, similarly to what the BE10 scale analysis had shown. The diabatic heating is responsible for γ decrease and EML demise when convection occurs, causing the temperature profile to tend toward the moist adiabatic lapse rate (BE10). Term B (Figs. 9b,g) indicate positive tendencies in γ over a broad area downstream of R1 in both continents. The positive horizontal advection of γ is greater over NA due to the greater γ gradient along the flow downstream of the EML plume in NA (Figs. 7a,d). Despite the lower values in comparison to NA, term B plays an important role in γ increase due to EML transport in SA. Poleward of R1 in SA, ascent (Figs. 7a) is responsible for negative γ tendency. Ascent is present poleward of R1 region in NA as well (Fig. 7d), but since term C is much lower than in SA (Figs. 9c,h), this suggests the EML γ in NA is nearly constant with height. This characteristic favors little or no γ decrease due to term C over NA as the EML travels downstream (Figs. 7f). The reduction in γ by ascent in SA is a factor contributing to lower γ over SA R3 (Fig. 7c), which is farther downstream from the Andes.

Term D (Figs. 9d,i) maximizes over the mountain ranges and immediately east of the highest peaks, in particular over the Andes. Among the non-advective terms (i.e., the terms responsible for γ change), term D presents positive values over a broader area just east of the highest peaks of the Andes, and is explored in more detail in this section.

Term E (Figs. 9e,j) has maxima and minima along the mountains and is relatively small to the east of the mountain ranges. Term E depends on the difference between γ and Γ_d, and is generally small within the EML (BE10).

We will next show a calculation of the two-dimensional mass streamfunction (Ψ_M) along selected longitudes to show the sense of the vertical circulation associated with EMLs (Fig. 10). Here, Ψ_M is given by:

$$\Psi_M = \frac{2\,\pi\,a\,\cos\varphi}{g}\int_0^p v\,dp\,, \qquad (2)$$

where a is the Earth's radius, φ is the latitude, g is gravity, p is the pressure and v is the meridional wind component (Townsend and Johnson 1985). The Ψ_M calculation method is described in Qin et al. (2006). We first show a pole-to-pole calculation of Ψ_M along 85ºW through the South Pacific subtropical anticyclone for the 133 spring cases when an EML was present east of the Andes (Fig. 10a). This calculation reveals that time-mean subsidence is present near 30ºS on the poleward side of the time-mean thermally direct Hadley circulation beneath the subtropical jet core (Fig. 10a). This time-mean subsidence near 30ºS is also a part of the equatorward branch of the time-mean thermally indirect circulation whose rising branch is centered near 60ºS (Fig. 10a). The Ψ_M calculation from 50º to 20ºS along 68ºW (AA' in Fig. 1a) immediately to the east of the Andes on the same 133 days when an EML is present shows that a thermally direct vertical circulation is present with an ascending branch equatorward of 30ºS beneath the subtropical jet core and a descending branch poleward of 40ºS on the cyclonic shear side of the subtropical jet core (Fig. 10b). A comparison of Figs. 10a and 10b reveals that transient synoptic-scale disturbances that cross the Andes can reverse the well-known time-mean Hadley circulation when EMLs are present. Also, the AA' cross section along 68ºW (Fig. 10b) depicts ageostrophic wind vectors that are oppositely directed to the northward-pointing horizontal θ gradient below 500 hPa between 20ºS and 30ºS. Above 500 hPa, the ageostrophic wind vectors point in the direction of the horizontal θ gradient. Accordingly, the ageostrophic winds beneath the subtropical jet core result warm-air advection in the 600-500-hPa layer and cold-air advection above 450 hPa with a resulting increase γ and a steepening of the mid-tropospheric lapse rate.

A latitudinal cross section along 28ºS (BB' in Fig. 1a) is shown in Fig. 10c. Low-level northeasterly ageostrophic winds that are located along the eastern Andes foothills are characteristic of a terrain-channeled northerly barrier jet. The approaching upper-level trough (Fig. 6a) induces low-level geopotential height falls east of the Andes (Fig. 8a; Seluchi et al. 2003). The associated terrain-channeled low-level northerly flow accelerates as convergence occurs along the eastern slopes of the Andes. Since the jet-induced thermally-direct circulation acts to oppose the observed ageostrophic winds east of the Andes during EML events (Fig. 10b), the terrain-channeled ageostrophic northerly flow east of the Andes and the associated warm advection are the main mechanisms for steepening lapse rates (γ increase).

3.2.3. Severe weather parameters

This section presents an ingredients-based analysis (Johns and Doswell 1992) of environments characterized by the presence EMLs over the R1–R3 regions. The mechanisms for thunderstorm initiation, dissipation and the influence of mesoscale circulations are not addressed in this study.

The highest MUCAPE in SA (Figs. 11a–c) is concentrated within the R1–R3 regions in all composites. MUCAPE is higher over R3 region (Fig. 11c) because of higher low-level moisture (not shown) than in R1 and R2 regions (Figs. 11a,b), even though γ is lower in R3 (Fig. 7a–c). The 1000–500-hPa wind shear increases poleward and is higher south of the R2 and R3 regions (Figs. 11b,c). The area of greatest ascent poleward of the regions (Figs. 7a–c) is characterized by higher 1000-500-hPa shear but considerably lower MUCAPE than over the R1–R3 regions. The highest CIN values (Figs. 11a–c) are located in the areas where the EMLs have lower base levels and are thicker (Fig. 3a) immediately to the east of the Andes. Reduced CIN values over R3 (Fig. 11c) in association with lower γ (Fig. 7c) are likely a result of EML dissipation as it is advected eastward.

MUCAPE distributions in NA composites (Figs. 11d–f) are comparably different from SA (Figs. 11a–c). High MUCAPE is not confined within the R1–R3 regions, but extends from the Gulf of Mexico northward to cover a large area. The northward transport of high-θ_e air by stronger low-level winds in NA (Fig. 8), in association with steeper γ in the EML (Fig. 7) in comparison to SA is responsible for higher values of MUCAPE. The 1000–500-hPa wind shear in NA is lower than in SA due to the weaker upper-level flow during spring (Figs. 3a,e). Poleward of the R1–R3 regions, both in SA and NA (Fig. 11), the 1000–500-hPa wind shear attains the lower threshold for supercell formation (15 m s^{-1}) in NA (e.g., Weisman and Klemp 1982; Thompson et al. 2003). CIN in NA composites (Figs. 11d–f) is higher than 200 J kg^{-1} over the R1–R3 regions, whereas CIN only exceeds 100 J kg^{-1} over SA R1–R3 regions (Figs. 11a–c). CIN values of this magnitude in both continents are prohibitive for convective initiation. However, convective initiation is unlikely to occur in the middle of the EML, where CIN is the highest, but near its lateral boundaries (Carlson and Ludlam 1968; Keyser and Carlson 1984; LW91). This is the case in the composites, which show ascent (Fig. 7) and MFC (Fig. 8) poleward of the EML location, where CIN is much lower. The presence of moderate CIN also prevents a high number of storms from forming and allows CAPE to increase before convective initiation begins (Bunkers et al. 2010).

The SRH is widely used to estimate the potential for rotating thunderstorms (supercells) in the environment (Droegemeier et al. 1993; Markowski and Richardson 2009). Since SRH values associated with anticyclonic turning winds with height in the Southern Hemisphere are negative, here we will use the SRH magnitude for SA for the sake of comparison with NA.

All composites present SRH03 greater than 170 m^2 s^{-2} over and/or near the R1–R3 regions (Fig. 12), with the exception of SA R3 (Fig. 12c). The main difference between SA and NA composites is on SBCAPE values, which are about two times higher in NA over the R1–R3 regions. The higher SBCAPE in NA is related to higher relative humidity and dewpoint temperatures in the PBL, as will be shown later, in association with higher γ in the EML. Moreover, only over NA is the concomitant occurrence of high values of SBCAPE and SRH03 within the area where the CIN is below 100 J kg-1 (Figs.

11d–e) observed.

A greater difference between SA and NA exists in the SRH01 distribution (Fig. 13). The greater zonal component of 1000–850-hPa wind shear (Fig. 13) over the R1–R3 regions in NA is related to a more rapid anticyclonic turning of the winds with height and higher SRH01 over NA, as will be shown later. The LCL height distribution in SA is marked by high LCLs near the Andes and in Northern Argentina, Paraguay and Bolivia, and heights below 1000 m only in southern Brazil and Uruguay. The highest SRH01 values are collocated with LCL heights below 1000 m in all NA composites [in particular over NA R1 (Fig. 13d)], indicating an environment with very low cloud bases and high SRH in the PBL. These parameters also suggest that thunderstorms forming in such environments, where synoptic-scale ascent and MFC are present (Figs. 7 and 8), have a higher likelihood of generating tornadoes near NA regions, where a combination of higher SRH01 and SBCAPE and lower LCL heights occurs (Thompson et al. 2003).

3.2.4. Soundings and hodographs

Composite soundings and hodographs were generated by using the gridpoint in the middle of the 5ºx5º areas of the R1–R3 regions (Fig. 14). The composite soundings and hodographs averaged over the 5ºx5º areas (not shown) give very similar results. The EML is evident in the temperature profile (Figs. 14a,b), its height varying between SA and NA, corroborating what was discussed in Section 3.1. Composite soundings in SA (Fig. 14a) show steep γ in the EML above a layer with less steep γ, between 700 and 600 hPa. The temperature inversion is better characterized in R1 (Fig. 14a), resulting in higher CIN in this location (Fig. 11a). In NA (Fig. 10b), the temperature inversion is more clear between 850 and 750 hPa. CFSR has difficulty in representing the temperature inversion in the base of EMLs (Fig. 2).

The low-level temperature/dew point temperature profiles in SA (Fig. 14a) exhibit an "inverted-V" shape, with relative humidity decreasing from 700 hPa to the surface, particularly in R1. Greater relative humidity is found near the surface in NA (Fig. 14b). The moist low-level layer in NA is much shallower than in SA, extending from surface to about 900 hPa, above which the drier air associated with the EML resides. Higher relative humidity due to lower temperature and higher dew point temperature in NA composite soundings is related to lower LCL height (Figs. 13c–e), which is an important characteristic observed in environments favoring tornadic thunderstorms (e.g., Rasmussen and Blanchard 1998; Thompson et al. 2003). The closer proximity of NA R1–R3 regions to the main moisture source (Gulf of Mexico) is one of the reasons for higher low-level RH in comparison to SA.

The composite hodographs in SA (Fig. 14c) exhibit anticyclonic turning of the winds from surface to nearly 700 hPa, indicating warm advection in this layer (Fig. 8). The higher SRH in NA (Figs. 12 and 13) is due to stronger poleward flow at 1000 hPa in association with stronger zonal component of the flow in 850 and 700 hPa, favoring a more pronounced anticyclonic turning of the winds with height in comparison with SA. In SA, the high elevation of the Andes precludes westerly low-level winds, in particular over R1 and R2 (Figs. 8a,b). SA R3 composite hodographs (Fig. 14c) depict stronger low-level zonal winds than R1-R2 composites because of the greater distance from the Andes, but the weaker meridional low-level winds cause lower SRH values relative to R1 and R2 composites (Figs. 12a–c and 13a–c).

3.2.5. Boxplots

Figure 15 shows boxplots of the distributions of the severe weather parameters (described in Sec. 2.3) for each region. The NA MUCAPE distribution (Fig. 15a) exhibits higher values of almost all statistical parameters when comparing a given region with its SA counterpart. A greater difference exists between both continents in the SBCAPE distributions (Fig. 15e), with considerably higher values in the NA regions. Both MUCAPE and SBCAPE differences between SA and NA are statistically significant (95% confidence) for R1 and R2. The lower EML bases in NA relate to CIN values nearly twice as large in SA (Fig. 15b). The LCL heights (Fig. 15f) in SA are relatively higher than in NA, except in R3. These distributions corroborate Figs. 9 and 10, showing lower mean LCL heights in NA and higher frequency of environments having LCL heights favorable for tornadic storms (Rasmussen and Blanchard 1998; Thompson et al. 2003).

Little difference exists between the distributions of 1000–850-hPa wind shear in SA and NA (Fig. 15c), despite relatively lower values in SA R3, which relates to lower SRH01 in this region (Fig. 15d). The 1000–500-hPa wind shear (Fig. 15g) is higher in NA R1 and SA R2. The average 1000–500-hPa wind shear is higher in SA poleward of the EML location (Fig. 11), where the ascent is greater (Fig. 7).

The SRH03 distributions (Fig. 15h) are very similar among continents, but the SRH01 distributions (Fig. 15d) exhibit higher (and statistically significant) values in NA. The SRH03 and SRH01 composite fields (Figs. 12 and 13) show that even higher SRH values are found poleward of the NA regions, not inside the 5ºx5º areas. Corroborating what the composite fields have shown (Figs. 12 and 13), R2 of SA has SRH comparable to NA regions (Fig. 15d) but considerably lower SBCAPE (Fig. 15e), which limits the likelihood for surface-based supercells and tornado occurrence for convective initiation occurring in these environments (Brooks et al. 2003; Smith et al. 2012; Thompson et al. 2012), based on the available ingredients.

The conclusions associated with Figs. 11–15 base on Smith et al. (2012) and Thompson et al. (2012), which show how the severe weather parameters link with convective modes and severe weather hazards. The present study is the first to relate the severe weather parameters with EMLs in SA and NA and to compare the parameters between both continents.

4. Concluding discussion

This paper presented a climatology of EMLs in NA and SA based on CFSR data. The method to identify EMLs was based on the occurrence of an elevated, 150-hPa-thick layer having at least 7.5 K km^{-1} of γ. The average characteristics of the EMLs, its seasonal variability and the synoptic-scale environments associated with EMLs were analyzed.

EML occurrence in SA peaks in winter in southern Paraguay and northeastern Argentina, and exhibits a minimum during summer in western Argentina. EML formation occurs in the anticyclonic shear side of the upper-level jet, and follows the jet seasonal meridional displacement. SA EMLs form due to ageostrophic circulations east of the Andes, mainly the terrain-channeled northerly flow caused by the lee low-pressure system ahead of the approaching upper-level trough, which increases γ by differential ageostrophic temperature advection. Greater baroclinicity during the cold season in SA enhances the effects of ageostrophic circulations in the γ change, and explains the higher frequency of EMLs east of the Andes from fall to spring. In NA, EML occurrence follows the maximum solar radiation over the higher terrain, with the maximum frequency in spring migrating northward in summer, similarly to the findings of other studies (e.g., LW91). The lower height of the Rockies in NA, as compared to the Andes, is responsible for EML bases nearly 100 hPa lower in NA, since the γ increase mechanisms are coupled to the mountain ranges in both continents. Greater EML thicknesses in NA are found in spring and summer, but during winter in SA. The formation of surface-based mixed layers through radiative heating over high terrain causes the EML characteristics over NA to be more homogeneous and less variable as the EML is advected away from the Rockies. On the other hand, SA EML characteristics are more heterogeneous due to the ageostrophic circulations responsible for γ increase (terms C, D and E), which are characterized by localized maxima and minima in the γ tendency field. It is important to note, however, that the estimation of the γ tendency equation terms based on composites of EML cases is not the most accurate method to study the

EML formation processes. An analysis of the terms along EML parcels trajectories, followed by a statistical analysis of the magnitude of each term, may provide more reliable results, and is a suggestion for future studies. Another suggestion is the use of idealized numerical modeling to study EML formation mechanisms.

Synoptic conditions associated with EML occurrence in both continents are characterized by an anomalous upper-level trough over the mountain ranges and an anomalous ridge downstream, which favors a southwesterly upper-level flow over the R1–R3 regions of NA and northwesterly flow over SA. The MFC associated with meridional θ_e gradient and ascent poleward of the R1–R3 regions indicate warm-front activity in this area. The amplitude of the upper-level flow is greater when EMLs occur at higher latitudes (over R2), which induces stronger poleward-directed low-level flow east of the mountains. EMLs advected farther east (over R3) present lower γ decrease in NA in comparison to SA, which is attributed to lower vertical γ advection and stretching (terms C and E) in NA because γ is higher. R3 in both continents are also characterized by greater zonal component of the low-level flow and consequently lower SRH, particularly over SA. The southwesterly upper-level flow regime in NA has been described by LW91 as the most common configuration for EML formation, but other synoptic flow regimes are related to EML occurrence. The composites in this paper do not deal with the different synoptic conditions that favor EMLs in SA and their seasonal variability, but provide a starting point for further studies on this theme. Climatological studies of EMLs in other parts of the world, such as near the Tibetan Plateau, are suggested.

Deep-layer shear is higher in SA in comparison to NA in general, due to the climatologically stronger upper-level jet in SA. However, greater PBL moisture superposed by higher γ cause both MUCAPE and SBCAPE to be higher in NA where EMLs occur, and there is a better collocation of the high-CAPE plume with high values of SRH, mainly in the 0–1-km layer. NA composites also present lower LCL heights due to higher relative humidity in the lowest levels above the ground. Composite hodographs for NA regions have stronger winds from 1000 to 850 hPa and a more rapid anticyclonic turning with height in comparison to SA composites, which explains the higher SRH in general. The distributions of the severe-weather parameters suggest a higher likelihood for supercells and tornadoes to form in NA in EML environments.

Some concerns about this research must be kept in mind. Brooks et al. (2003) point that the analysis of severe weather environments based entirely on the available ingredients (Johns and Doswell 1992) might be missing important information. Reanalyses do not characterize mesoscale boundaries correctly, and research has shown that these boundaries are very important to the generation and modification of existing vorticity in the environment, allowing mesocyclogenesis and tornadogenesis to occur (e.g., Markowski and Richardson 2009). The storm initiation mechanisms are also very important in the evolution of severe thunderstorms. The lack a severe weather report database in SA hinders more conclusive results regarding the association of the EML environments with severe thunderstorms (Nascimento and Doswell 2006). Recently, Nesbitt et al. (2016) and Rasmussen and Houze (2011; 2016) presented evidence of the occurrence of squall lines and supercells in western Argentina (in some occasions associated with EMLs), but a long climatological study that associates the environmental conditions with observed severe storm reports is necessary in SA.

We hope that future field campaigns, like the RELAMPAGO Project (webpage: https://publish.illinois.edu/relampago/) in northwestern Argentina, scheduled for November-December of 2018, will elucidate some aspects of EML formation near the Andes and their relation with severe thunderstorms in the region by using an observational network instead of reanalysis data. Also, there is an evident need for improvement of SA soundings network, mainly in areas in northern Argentina, Paraguay and Bolivia. Soundings in these areas will capture important features in the severe weather environments east of the Andes, such as the low-level jet and the EML, improving forecasts and increasing our understanding of the weather in this region.

Acknowledgements

The first author acknowledges support from *CNPq - Ciência Sem Fronteiras* program (233142/2014-2), from Brazil, and the Department of Atmospheric and Environmental Sciences of the University at Albany for the research and computational support. The second author acknowledges research support from NSF Grant AGS-1240502. We acknowledge the editor and three anonymous reviewers for their enormous contribution to the quality of this paper.

References

Anabor, V., D. J. Stensrud, and O. L. de Moraes, 2008: Serial upstream-propagating mesoscale convective system events over southeastern South America. *Mon. Wea. Rev.*, **136**, 3087–3105, doi:10.1175/2007MWR2334.1.

Banacos, P. C., and D. M. Schultz, 2005: The use of moisture flux convergence in forecasting convective initiation: Historical and operational perspectives. Wea. Forecasting, **20**, 351–366, doi:10.1175/WAF858.1.

_____, and M. L. Ekster, 2010: The association of the elevated mixed layer with significant severe weather events in the Northeastern United States. *Wea. Forecasting*, 25, 1082–1102, doi:10.1175/2010WAF2222363.1.

Bao, X., and F. Zhang, 2013: Evaluation of NCEP–CFSR, NCEP–NCAR, ERA-Interim, and ERA-40 reanalysis datasets against independent sounding observations over the Tibetan Plateau. *J. Climate*, **26**, 206-214, doi:10.1175/JCLI-D-12-00056.1.

Brooks, H. E., J. W. Lee, and J. P. Craven, 2003: The spatial distribution of severe thunderstorm and tornado environments from global reanalysis data. *Atmos. Res.*, **67**, 73–94, doi:10.1016/S0169-8095(03)00045-0.

Bunkers, M. J., J. R. Wetenkamp Jr, J. J. Schild, and A. Fischer, 2010: Observations of the relationship between 700-mb temperatures and severe weather reports across the contiguous United States. *Wea. Forecasting*, **25**, 799–814, doi:10.1175/2009WAF2222333.1.

Carlson, T. N., and F. H. Ludlam, 1968: Conditions for the occurrence of severe local thunderstorms. *Tellus*, **20**, 203–226, doi:10.1111/j.2153-3490.1968.tb00364.x.

Chen, G., T. Iwasaki, H. Qin, and W. Sha, 2014: Evaluation of the warm-season diurnal variability over East Asia in recent reanalyses JRA-55, ERA-Interim, NCEP CFSR, and NASA MERRA. *J. Climate*, **27**, 5517-5537, doi:10.1175/JCLI-D-14-00005.1.

Cordeira, J. M., N. D. Metz, M. E. Howarth, and T. J. Galarneau, 2017: Multiscale upstream and in situ precursors to the elevated mixed layer and high-impact weather over the Midwest United States. *Wea. Forecasting*, **32**, 905-923.

Das, S., U. C. Mohanty, A. Tyagi, D. R. Sikka, P. V. Joseph, L. S. Rathore, A. Habib, K. Baidya, K. Sonam, and A. Sarkar, 2014: The SAARC STORM: a coordinated field experiment on severe thunderstorm observations and regional modeling over the South Asian Region. *Bull. Amer. Meteor. Soc.*, **95**, 603–617, doi:10.1175/BAMS-D-12-00237.1.

Davies, J. M., and R. H. Johns, 1993: Some wind and instability parameters associated with strong and violent tornadoes: 1. Wind shear and helicity. *The Tornado: Its Structure, Dynamics, Prediction, and Hazards, Geophys. Monogr.,* Vol. 79, Amer. Geophys. Union, 573–582, doi:10.1029/GM079p0573.

Droegemeier, K. K., S. M. Lazarus, and R. Davies-Jones, 1993: The influence of helicity on numerically simulated convective thunderstorms. *Mon. Wea. Rev.*, **121**, 2005–2029, doi:10.1175/1520-0493(1993)121<2005:TIOHON>2.0.CO;2.

Johns, R. H., and C. A. Doswell, 1992: Severe local storms forecasting. *Wea. Forecasting*, **7**, 588–612, doi:10.1175/1520-0434(1992)007<0588:SLSF>2.0.CO;2.

Keyser, D., and T. N. Carlson, 1984: Transverse ageostrophic circulations associated with elevated mixed layers. *Mon. Wea. Rev.*, **112**, 2465–2478, doi:10.1175/1520-0493(1984)112<2465:TACAWE>2.0.CO;2.

Lanicci, J. M., and T. T. Warner, 1991a: A synoptic climatology of the elevated mixed-layer inversion over the southern Great Plains in spring. Part I: Structure, dynamics, and seasonal evolution. *Wea. Forecasting*, **6**, 181–197, doi:10.1175/1520-0434(1991)006<0181:ASCOTE>2.0.CO;2.

_____, and _____, 1991b: A synoptic climatology of the elevated mixed-layer inversion over the southern Great Plains in spring. Part II: The life cycle of the lid. *Wea. Forecasting*, **6**, 198–213, doi:10.1175/1520-0434(1991)006<0198:ASCOTE>2.0.CO;2.

_____, and _____, 1991c: A synoptic climatology of the elevated mixed-layer inversion over the southern Great Plains in spring. Part III: Relationship to severe-storms climatology. *Wea. Forecasting*, **6**, 214–226, doi:10.1175/1520-0434(1991)006<0214:ASCOTE>2.0.CO;2.

Lawrence, M. G., 2005: The relationship between relative humidity and the dewpoint temperature in moist air: A simple conversion and applications. *Bull. Amer. Meteor. Soc.*, **86**, 225–233, doi:10.1175/BAMS-86-2-225.

Machado, L. A. T., W. B. Rossow, R. L. Guedes, and A. W. Walker, 1998: Life cycle variations of mesoscale convective systems over the Americas. *Mon. Wea. Rev.*, **126**, 1630–1654, doi:10.1175/1520-0493(1998)126<1630:LCVOMC>2.0.CO;2.

Markowski, P. M., and Y. P. Richardson, 2009: Tornadogenesis: Our current understanding, forecasting considerations, and questions to guide future research. *Atmos. Res.*, **93**, 3–10, doi:10.1016/j.atmosres.2008.09.015.

Nascimento, E. L., and C. A. Doswell III, 2006: The need for an improved documentation of severe thunderstorms and tornadoes in South America. *Symp. on* *the Challenges of Severe Convective Thunderstorms: 86th Annual Meeting*, Atlanta, GA, Amer. Meteor. Soc. [Available online at https://ams.confex.com/ams/pdfpapers/102247.pdf.]

Nesbitt, S. W., P. Borque, K. L. Rasmussen, P. Salio, R. J. Trapp, L. Vidal, M. Rugna, and J. Mulholland, 2016: Severe convection in Central Argentina: Storm modes and environments. Preprints, *28th Conf. Severe Local Storms*, Portland, OR, Amer. Meteor. Soc. [Available online at https://ams.confex.com/ams/28SLS/webprogram/Paper301960.html.]

Qin, Y., P. Wang, Z. Guan, and Y. Yue, 2006: Comparison of the Hadley cells calculated from two reanalysis data sets. *Chinese Science Bulletin*, **51**, 1741–1746, doi:10.1007/s11434-006-2030-3.

Rasmussen, E. N., and D. O. Blanchard, 1998: A baseline climatology of sounding-derived supercell and tornado forecast parameters. *Wea. Forecasting*, **13**, 1148–1164, doi:10.1175/1520-0434(1998)013<1148:ABCOSD>2.0.CO;2.

Rasmussen, K. L., and R. A. Houze Jr., 2011: Orogenic convection in subtropical South America as seen by the TRMM satellite. *Mon. Wea. Rev.*, **139**, 2399–2420, doi:10.1175/MWR-D-10-05006.1.

_____, and R. A. Houze Jr., 2016: Convective initiation near the Andes in subtropical South America. *Mon. Wea. Rev.*, **144**, 2351-2374, doi:10.1175/MWR-D-15-0058.1.

Saha, S., and Coauthors, 2010: The NCEP climate forecast system reanalysis. *Bull. Amer. Meteor. Soc.*, *91*(8), 1015–1057, doi:10.1175/2010BAMS3001.1.

Salio, P., M. Nicolini, and E. J. Zipser, 2007: Mesoscale convective systems over southeastern South America and their relationship with the South American low-level jet. *Mon. Wea. Rev.*, **135**, 1290–1309, doi:10.1175/MWR3305.1.

Seluchi, M. E., A. C. Saulo, M. Nicolini, and P. Satyamurty, 2003: The northwestern Argentinean low: A study of two typical events. *Mon. Wea. Rev.*, **131**, 2361–2378, doi:10.1175/1520-0493(2003)131<2361:TNALAS>2.0.CO;2.

Smith, B. T., R. L. Thompson, J. S. Grams, C. Broyles and H. E. Brooks, 2012: Convective modes for significant severe thunderstorms in the contiguous United States. Part I: Storm classification and climatology. *Wea. Forecasting*, **27**, 1114–1135, doi:10.1175/WAF-D-11-00115.1.

Thompson, R. L., R. Edwards, J. A. Hart, K. L. Elmore, and P. Markowski, 2003: Close proximity soundings within supercell environments obtained from the Rapid Update Cycle. *Wea. Forecasting*, **18**, 1243–1261, doi:10.1175/1520-0434(2003)018<1243:CPSWSE>2.0.CO;2.

Thompson, R. L., B. L. Smith, J. S. Grams, A. R. Dean, and C. Broyles, 2012: Convective modes for significant severe thunderstorms in the contiguous United States. Part II: Supercell and QLCS tornado environments. *Wea. Forecasting*, **27**, 1136-1154, doi:10.1175/WAF-D-11-00116.1.

Townsend, R. D., and D. R. Johnson, 1985: A diagnostic study of the isentropic zonally averaged mass circulation during the first GARP global experiment. *J. Atmos. Sci.*, **42**, 1565-1579, doi: 10.1175/1520-0469(1985)042<1565:ADSOTI>2.0.CO;2.

Uccellini, L. W., D. R. and Johnson, 1979: The coupling of upper and lower tropospheric jet streaks and implications for the development of severe convective thunderstorms. *Mon. Wea. Rev.*, **107**, 682–703, doi:10.1175/1520-0493(1979)107<0682:TCOUAL>2.0.CO;2.

Velasco, I., and J. M. Fritsch, 1987: Mesoscale convective complexes in the Americas. *Journal of Geophysical Research: Atmospheres*, **92**, 9591-9613, doi:10.1029/JD092iD08p09591.

Weisman, M. L., and J. B. Klemp, 1982: The dependence of numerically simulated convective thunderstorms on vertical wind shear and buoyancy. *Mon. Wea. Rev.*, **110**, 504–520, doi:10.1175/1520-0493(1982)110<0504:TDONSC>2.0.CO;2.

Zipser, E. J., D. J. Cecil, C. Liu, S. W. Nesbitt, and D. P. Yorty, 2006: Where are the most intense thunderstorms on Earth? *Bull. Amer. Meteor. Soc.*, **87**, 1057–1071, doi:10.1175/BAMS-87-8-1057.

Tables:

TABLE 1: Averages and standard deviations (st. dev.) of the differences between observed EML soundings and CFSR EML soundings. A positive average result from higher value of the parameter in observed soundings. Bold values indicate statistically significant differences between observed and CFSR soundings. Four stations in SA and four in NA are shown as examples.

Station	Soundings	EML base (hPa)		EML thickness (hPa)		EML γ (K km^{-1})		EML θ (K)	
		Average	St. dev.	Average	St. dev.	Average	St. dev.	Average	St. dev.
SACO	33	3.15	46.77	**-39.67**	**73.23**	**0.60**	**0.32**	-0.23	3.03
SARE	42	8.99	41.33	-22.81	70.23	**0.75**	**0.45**	-1.52	2.35
SBFI	140	15.69	47.17	-2.51	53.23	**0.45**	**1.04**	-1.10	2.57
SBUG	96	17.44	48.00	-18.19	84.60	**0.47**	**0.74**	-0.98	2.52
OUN	346	0.27	43.16	**-11.87**	**61.51**	**0.74**	**0.46**	-0.57	2.12
FWD	488	4.95	41.37	**-7.17**	**64.47**	**0.66**	**0.46**	-0.50	1.99
TOP	377	-3.76	44.94	**-16.51**	**66.01**	**0.67**	**0.49**	**-0.79**	**2.54**
OAX	273	-3.43	45.41	**-12.00**	**56.67**	0.67	0.42	-0.39	1.83
Total	6214	1.03	45.63	**-15.26**	**64.79**	**0.68**	**0.49**	**-0.55**	**2.21**

Figures caption list:

FIG. 1. Study areas (grey squares) in (a) SA and (b) NA. Orography is shaded every 500 m starting at 1500 m. The black squares show the three 5ºx5º regions, in each continent, used in the composites (details in the text). The names of the sounding sites located within the study areas are shown in blue. The AA' and BB' lines depict the location of the cross sections in Fig. 10. The borders of the states of the Unites States and Brazil are shown in thinner grey contours.

FIG. 2. Observed (red) and CFSR (blue) EML soundings at (a) Cordoba (SACO), Argentina, at 0000 UTC 1 April 2015, (b) Santa Maria (SBSM), Brazil, at 0000 UTC 7 October 2015, (c) Fort Worth (FWD), TX, Unites States, at 1200 UTC 9 April 2015 and Omaha (OAX), NE, Unites States, at 0000 UTC 24 May 2010. Figure 1 shows the locations of the sounding sites. The colored dashes indicate the EML bases in each sounding. CFSR soundings were taken in the closest gridpoint relative to the station coordinates.

FIG. 3. Percentage of synoptic times with EML (%, shaded) and mean seasonal 250-hPa wind speed (m s^{-1}, black contours every 2 m s^{-1} starting at 20 m s^{-1}) for (a) spring, (b) summer, (c) fall and (d) winter in SA and (e) spring, (f) summer, (g) fall and (h) winter in NA. Orography is shaded every 500 m starting at 1500 m. Black points are the sounding sites.

FIG. 4. Mean EML base level (hPa, shaded) and mean EML thickness (hPa, black contours every 10 hPa) for (a) spring, (b) summer, (c) fall and (d) winter in SA and (e) spring, (f) summer, (g) fall and (h) winter in NA. All variables are plotted only in gridpoints with percentages (as in Fig. 2) greater than 4%. Orography is shaded every 500 m starting in 1500 m. Black points are the sounding sites.

FIG. 5. Mean EML γ (K km^{-1}, shaded) and θ (K, black contours every 2 K) for (a) spring, (b) summer, (c) fall and (d) winter in SA and (e) spring, (f) summer, (g) fall and (h) winter in NA. All variables are plotted only in gridpoints with percentages (as in Fig. 2) greater than 4%. Orography is shaded every 500 m starting in 1500 m. Black points are the sounding sites.

FIG. 6. Composite 250-hPa wind speed (m s^{-1}, shaded), geopotential height (dam, black contours every 12 dam) and standardized anomalies of geopotential height [red contours for positive anomalies every 0.25 standard deviation starting in +0.25 standard deviation and blue contours for negative anomalies every –0.25 standard deviation starting in -0.25 standard deviation] for EML cases in spring in (a) R1, (b) R2 and (c) R3 of SA and (d) R1, (e) R2 and (f) R3 of NA. The brown contour shows the 1500-m orographic contour. The 5ºx5º areas are drawn in green squares.

FIG. 7. Composite ω (10^{-2} Pa s^{-1}, shaded), γ (colored contours of 7, 7.5, 8 and 8.5 K km^{-1}) and wind (m s^{-1}, pennant is 25 m s^{-1}, full barb is 5 m s^{-1}, and half barb is 2.5 m s^{-1}; only wind barbs greater than 5 m s^{-1} are plotted), for EML cases in spring in (a) R1, (b) R2 and (c) R3 of SA and (d) R1, (e) R2 and (f) R3 of NA. The variables are averaged over the 600–400-hPa layer in SA and 700–500-hPa layer in NA. The brown contour shows the 1500-m orographic contour. The 5ºx5º areas are drawn in green squares.

FIG. 8. Composite 850-hPa θ_e (K, shaded), wind (m s^{-1}, pennant is 25 m s^{-1}, full barb is 5 m s^{-1}, and half barb is 2.5 m s^{-1}; only wind barbs greater than 5 m s^{-1} are plotted), and geopotential height (dam, black contours every 2 dam) and 1000–800-hPa MFC (10^{-5} g kg^{-1} s^{-1}, white contours every 4 x 10^{-5} g kg^{-1} s^{-1}) for EML cases in spring in (a) R1, (b) R2 and (c) R3 of SA and (d) R1, (e) R2 and (f) R3 of NA. Orography is shaded every 500 m starting in 1500 m. The 5ºx5º areas are drawn in green squares.

FIG. 9. γ tendency equation (a) term A, (b) term B, (c) term C, (d) term D, (e) term E in SA and (f) term A, (g) term B, (h) term C, (i) term D, (j) term E in NA (10^{-9} K m^{-1} s^{-1}, shaded). The terms are calculated from the composite fields of EML cases over R1 of each continent (gray squares) during spring, and are averaged over the 600–400-hPa layer in SA and 700–500-hPa layer in NA. The brown contour shows the 1500-m orographic contour.

FIG. 10. (a) Cross section from 90ºS to 90ºN along 85ºW of zonal wind magnitude (m s^{-1}, shaded), Ψ_M [10^{11} kg s^{-1}, negative values (anticlockwise circulation) in blue contours every –2 x 10^{11} kg s^{-1} starting at –1 x 10^{11} kg s^{-1}, and positive values (clockwise circulation) in red contours every 2 x 10^{11} kg s^{-1} starting at 1 x 10^{11} kg s^{-1}] and

θ (K, grey contours every 10 K). (b) Cross section of zonal wind magnitude (m s^{-1}, shaded), θ (K, grey contours every 10 K), Ψ_M (10^{11} kg s^{-1}, negative values in blue contours every –2 x 10^{11} kg s^{-1} starting at –1 x 10^{11} kg s^{-1}, and positive values in red contours every 2 x 10^{11} kg s^{-1} starting at 1 x 10^{11} kg s^{-1}), and meridional ageostrophic wind (m s^{-1}, vectors) along the AA' line (68ºW) in Fig. 1a. (c) Cross section of meridional ageostrophic wind with negative (positive) values denoting northerly (southerly) flow (m s^{-1}, shaded), θ (K, grey contours every 5 K), ω [10^{-2} Pa s^{-1}, negative values (ascent) in blue contours every –10 x 10^{-2} Pa s^{-1}, positive values (subsidence) in red contours every 10 x 10^{-2} Pa s^{-1}] along the BB' line (28ºS) in Fig. 1a.

FIG. 11. Composite MUCAPE (J kg^{-1}, shaded), 1000–500-hPa wind shear (m s^{-1}, pennant is 25 m s^{-1}, full barb is 5 m s^{-1}, and half barb is 2.5 m s^{-1}; only wind barbs greater than 10 m s^{-1} are plotted), and CIN (J kg^{-1}, dark red contours every -50 J kg^{-1} starting in -50 J kg^{-1}) for EML cases in spring in (a) R1, (b) R2 and (c) R3 of SA and (d) R1, (e) R2 and (f) R3 of NA. Orography is shaded every 500 m starting in 1500 m. The 5ºx5º areas are drawn in grey squares.

FIG. 12. Composite 0–3-km SRH magnitude (m^2 s^{-2}, shaded), 1000–700-hPa wind shear (m s^{-1}, pennant is 25 m s^{-1}, full barb is 5 m s^{-1}, and half barb is 2.5 m s^{-1}; only wind barbs greater than 5 m s^{-1} are plotted), and SBCAPE (J kg^{-1}, red contours every 300 J kg^{-1} starting in 300 J kg^{-1}) for EML cases in spring in (a) R1, (b) R2 and (c) R3 of SA and (d) R1, (e) R2 and (f) R3 of NA. Orography is shaded every 500 m starting in 1500 m. The 5ºx5º areas are drawn in blue squares.

FIG. 13. Composite 0–1-km SRH magnitude (m^2 s^{-2}, shaded), 1000–850-hPa

wind shear (m s^{-1}, pennant is 25 m s^{-1}, full barb is 5 m s^{-1}, and half barb is 2.5 m s^{-1}; only wind barbs greater than 2.5 m s^{-1} are plotted), and LCL height (m, colored contours every 300 m starting at 700 m) for EML cases in spring in (a) R1, (b) R2 and (c) R3 of SA and (d) R1, (e) R2 and (f) R3 of NA. Orography is shaded every 500 m starting in 1500 m. The 5ºx5º areas are drawn in blue squares.

FIG. 14. Composite soundings and hodographs for R1 (blue lines), R2 (red lines) and R3 (green lines) of (a, b) SA and (c, d) NA in spring. The colored stars in the maps are the locations of the soundings and hodographs in the middle of the 5°x5° areas. EML bases are indicated by colored dashes for each sounding. In the hodographs, storm motion is represented by the operator symbols with the same colors, circles of same wind speed are shown every 5 m s^{-1}, and the dark red, red, magenta, light blue and blue dots mark the 1000, 850, 700, 500 and 250-hPa levels, respectively.

FIG. 15. Boxplots of the distributions of (a) MUCAPE (J kg^{-1}), (b) CIN (J kg^{-1}), (c) 1000–850-hPa wind shear magnitude (m s^{-1}), (d) 0–1-km SRH magnitude (m^2 s^{-2}), (e) SBCAPE (J kg^{-1}), (f) LCL height (m), (g) 1000–500-hPa wind shear magnitude (m s^{-1}) and (h) 0–3-km SRH magnitude (m^2 s^{-2}) over the R1-R3 regions of SA (blue boxplots) and NA (red boxplots) in EML cases during spring. Statistical parameters in the boxplot are the 90^{th} and 10^{th} percentiles (upper and lower tickmarks, respectively), 75^{th} and 25^{th} percentiles (upper and lower boxes boundaries, respectively) and median (line inside the boxes). Parameters that present statistically significant (95% confidence) differences between the same regions in the continents are marked with an astherisk (*) in the x axis. Details about the construction of the boxplots are found in the text.

Figure 1

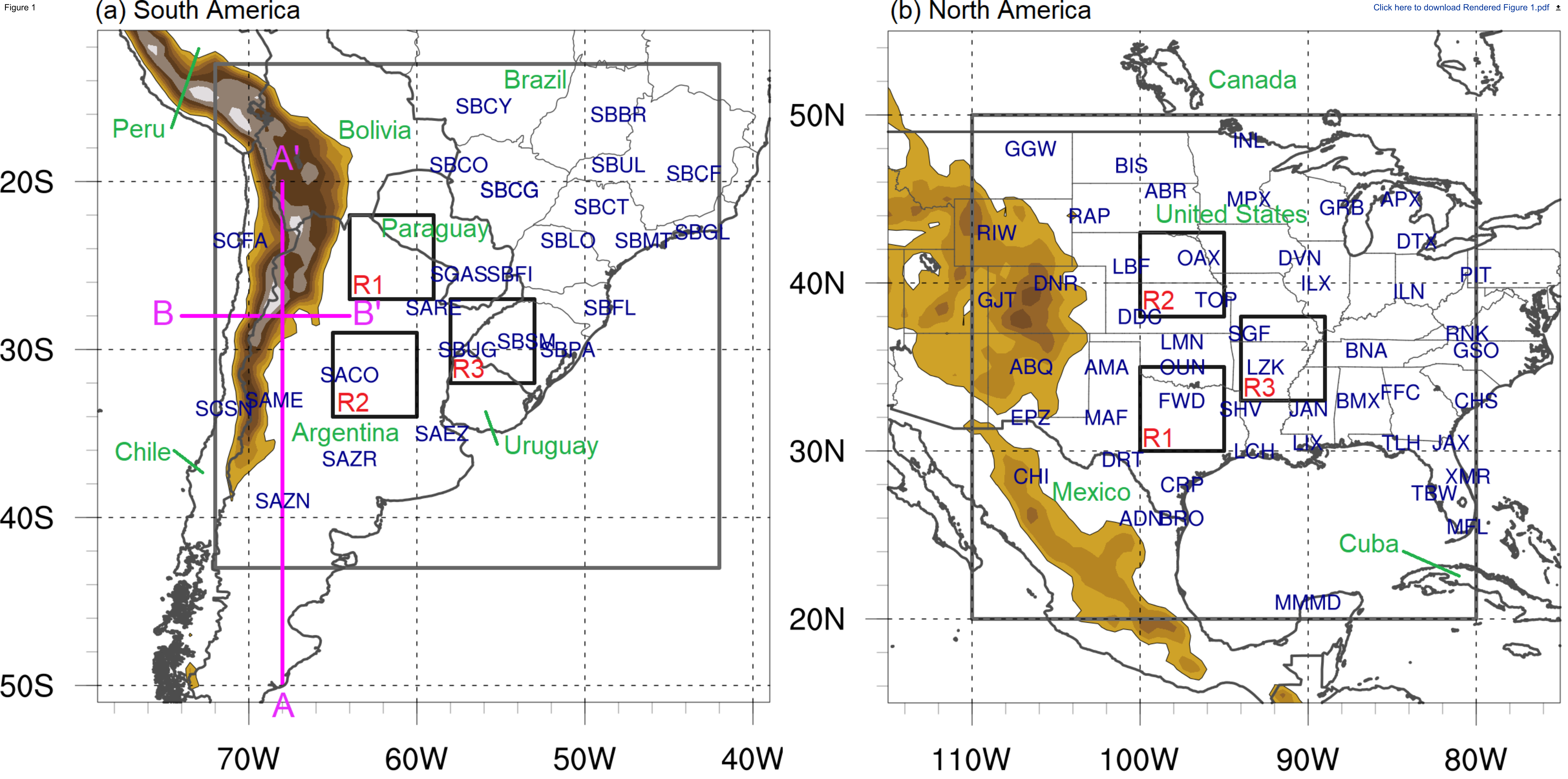

FIG. 1. Study areas (grey squares) in (a) SA and (b) NA. Orography is shaded every 500 m starting at 1500 m. The black squares show the three 5ºx5º regions, in each continent, used in the composites (details in the text). The names of the sounding sites located within the study areas are shown in blue. The AA' and BB' lines depict the location of the cross sections in Fig. 10. The borders of the states of the Unites States and Brazil are shown in thinner grey contours.

Figure 2

Click here to download Rendered Figure 2.pdf

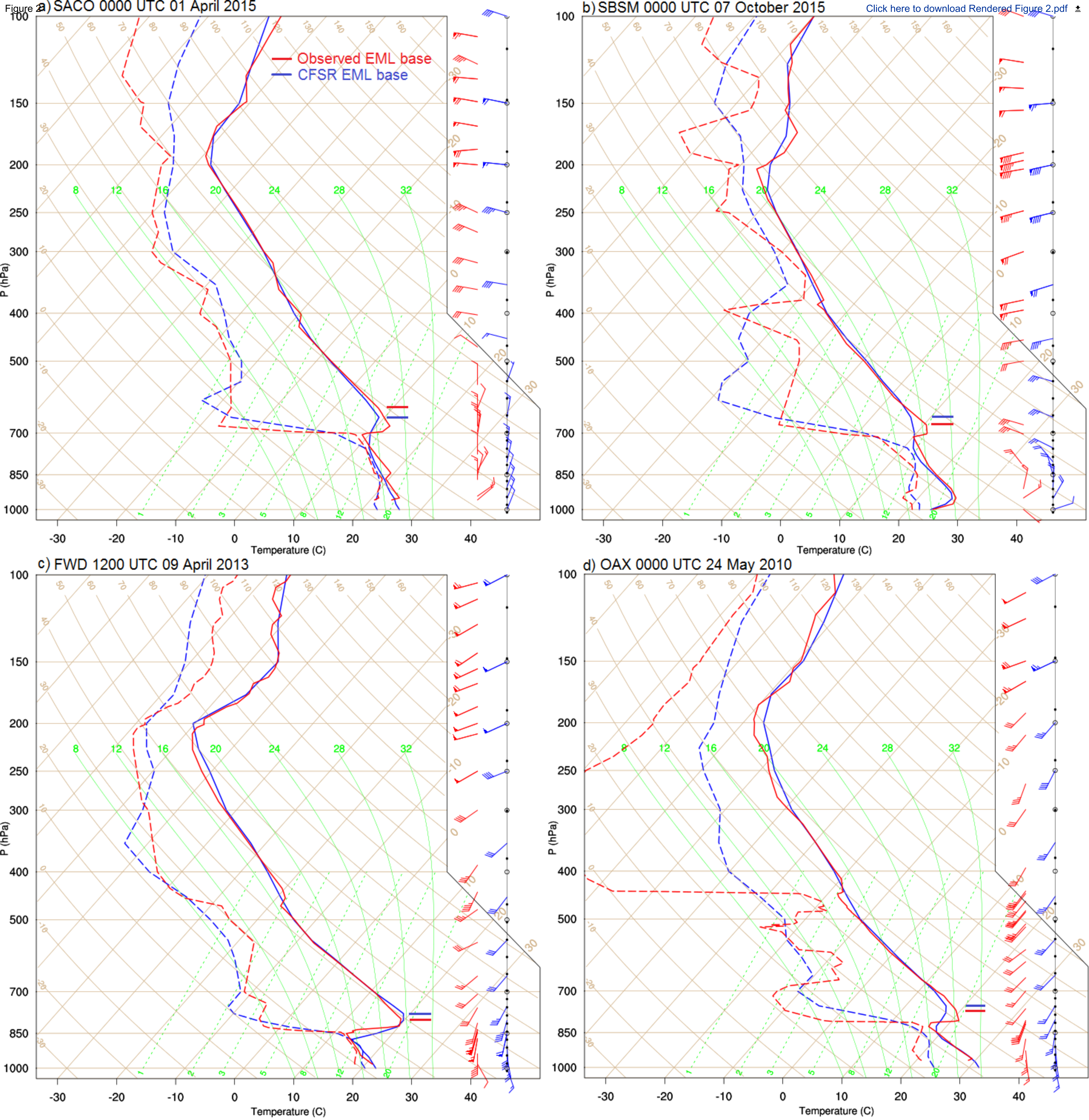

FIG. 2. Observed (red) and CFSR (blue) EML soundings at (a) Cordoba (SACO), Argentina, at 0000 UTC 1 April 2015, (b) Santa Maria (SBSM), Brazil, at 0000 UTC 7 October 2015, (c) Fort Worth (FWD), TX, Unites States, at 1200 UTC 9 April 2015 and Omaha (OAX), NE, Unites States, at 0000 UTC 24 May 2010. Figure 1 shows the locations of the sounding sites. The colored dashes indicate the EML bases in each sounding. CFSR soundings were taken in the closest gridpoint relative to the station coordinates.

FIG. 3. Percentage of synoptic times with EML (%, shaded) and mean seasonal 250-hPa wind speed (m s^{-1}, black contours every 2 m s^{-1} starting at 20 m s^{-1}) for (a) spring, (b) summer, (c) fall and (d) winter in SA and (e) spring, (f) summer, (g) fall and (h) winter in NA. Orography is shaded every 500 m starting at 1500 m. Black points are the sounding sites.

Figure 4

FIG. 4. Mean EML base level (hPa, shaded) and mean EML thickness (hPa, black contours every 10 hPa) for (a) spring, (b) summer, (c) fall and (d) winter in SA and (e) spring, (f) summer, (g) fall and (h) winter in NA. All variables are plotted only in gridpoints with percentages (as in Fig. 2) greater than 4%. Orography is shaded every 500 m starting in 1500 m. Black points are the sounding sites.

FIG. 5. Mean EML γ (K km^{-1}, shaded) and θ (K, black contours every 2 K) for (a) spring, (b) summer, (c) fall and (d) winter in SA and (e) spring, (f) summer, (g) fall and (h) winter in NA. All variables are plotted only in gridpoints with percentages (as in Fig. 2) greater than 4%. Orography is shaded every 500 m starting in 1500 m. Black points are the sounding sites.

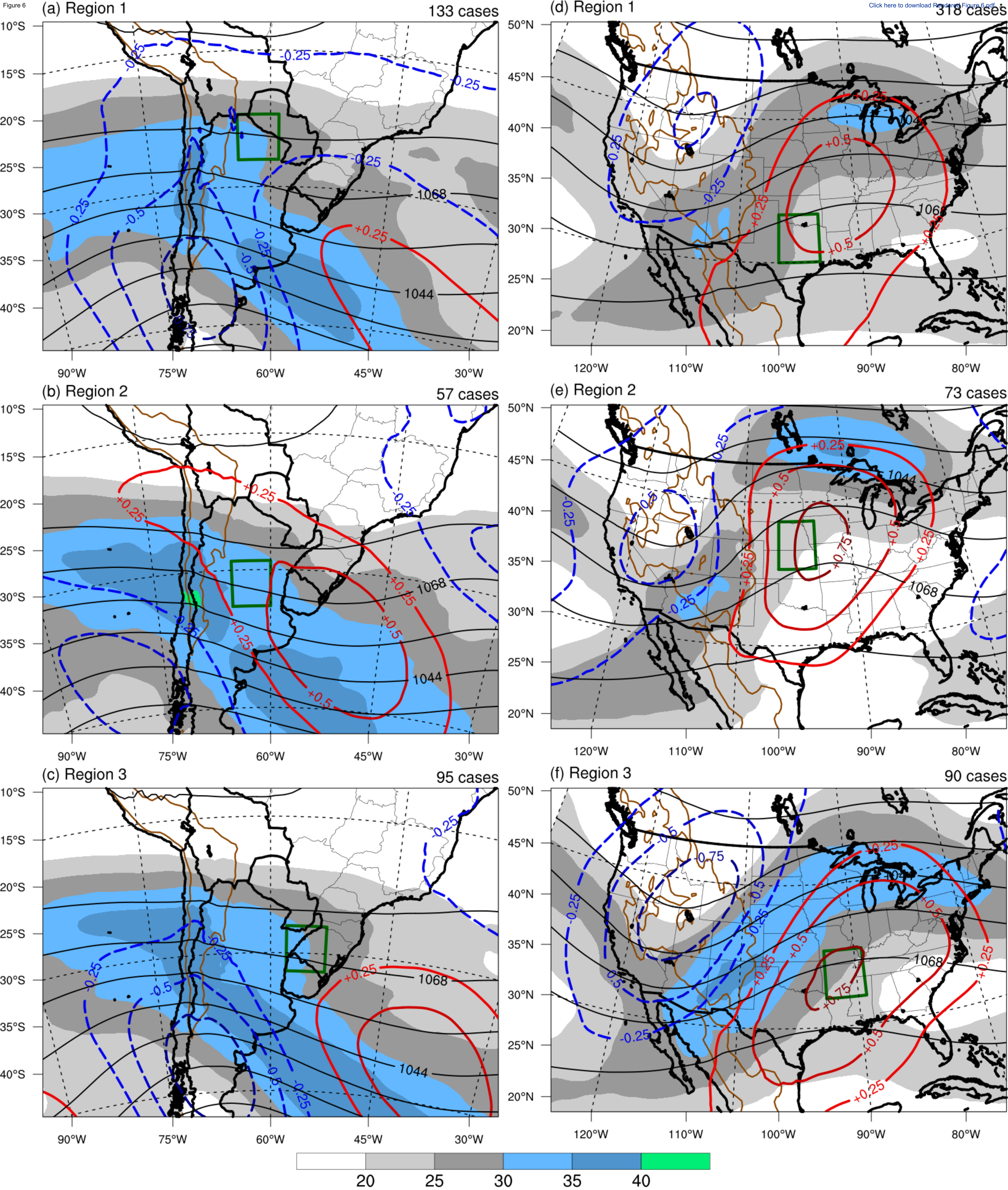

FIG. 6. Composite 250-hPa wind speed (m s^{-1}, shaded), geopotential height (dam, black contours every 12 dam) and standardized anomalies of geopotential height [red contours for positive anomalies every 0.25 standard deviation starting in +0.25 standard deviation and blue contours for negative anomalies every –0.25 standard deviation starting in -0.25 standard deviation] for EML cases in spring in (a) R1, (b) R2 and (c) R3 of SA and (d) R1, (e) R2 and (f) R3 of NA. The brown contour shows the 1500-m orographic contour. The 5ºx5º areas are drawn in green squares.

Figure 7

FIG. 7. Composite ω (10^{-2} Pa s^{-1}, shaded), γ (colored contours of 7, 7.5, 8 and 8.5 K km^{-1}) and wind (m s^{-1}, pennant is 25 m s^{-1}, full barb is 5 m s^{-1}, and half barb is 2.5 m s^{-1}; only wind barbs greater than 5 m s^{-1} are plotted), for EML cases in spring in (a) R1, (b) R2 and (c) R3 of SA and (d) R1, (e) R2 and (f) R3 of NA. The variables are averaged over the 600–400-hPa layer in SA and 700–500-hPa layer in NA. The brown contour shows the 1500-m orographic contour. The 5°x5° areas are drawn in green squares.

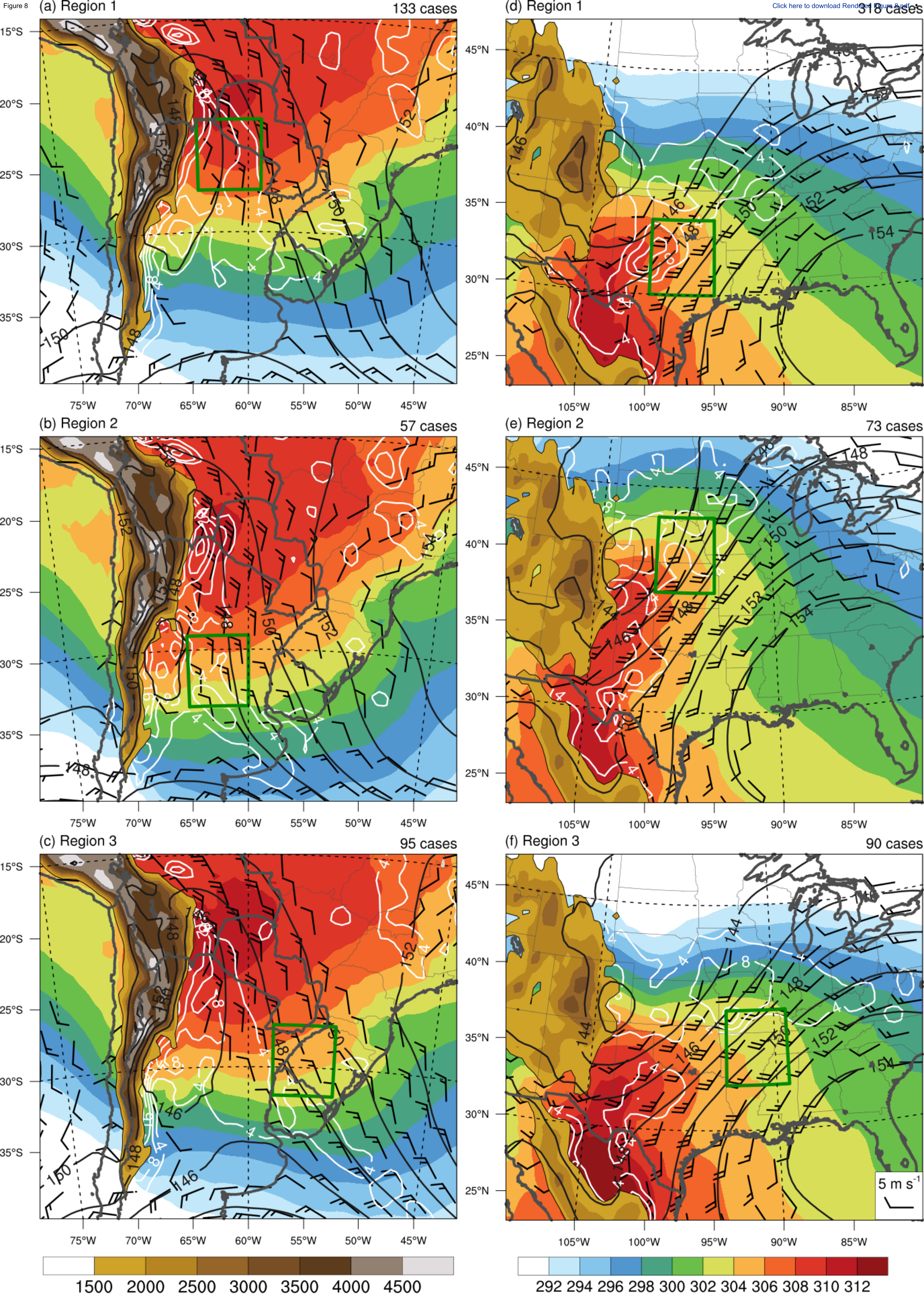

FIG. 8. Composite 850-hPa θe (K, shaded), wind (m s^{-1}, pennant is 25 m s^{-1}, full barb is 5 m s^{-1}, and half barb is 2.5 m s^{-1}; only wind barbs greater than 5 m s^{-1} are plotted), and geopotential height (dam, black contours every 2 dam) and 1000–800-hPa MFC (10^{-5} g kg^{-1} s^{-1}, white contours every 4 x 10^{-5} g kg^{-1} s^{-1}) for EML cases in spring in (a) R1, (b) R2 and (c) R3 of SA and (d) R1, (e) R2 and (f) R3 of NA. Orography is shaded every 500 m starting in 1500 m. The 5º×5º areas are drawn in green squares.

Figure 9

Click here to download Rendered Figure 9.pdf

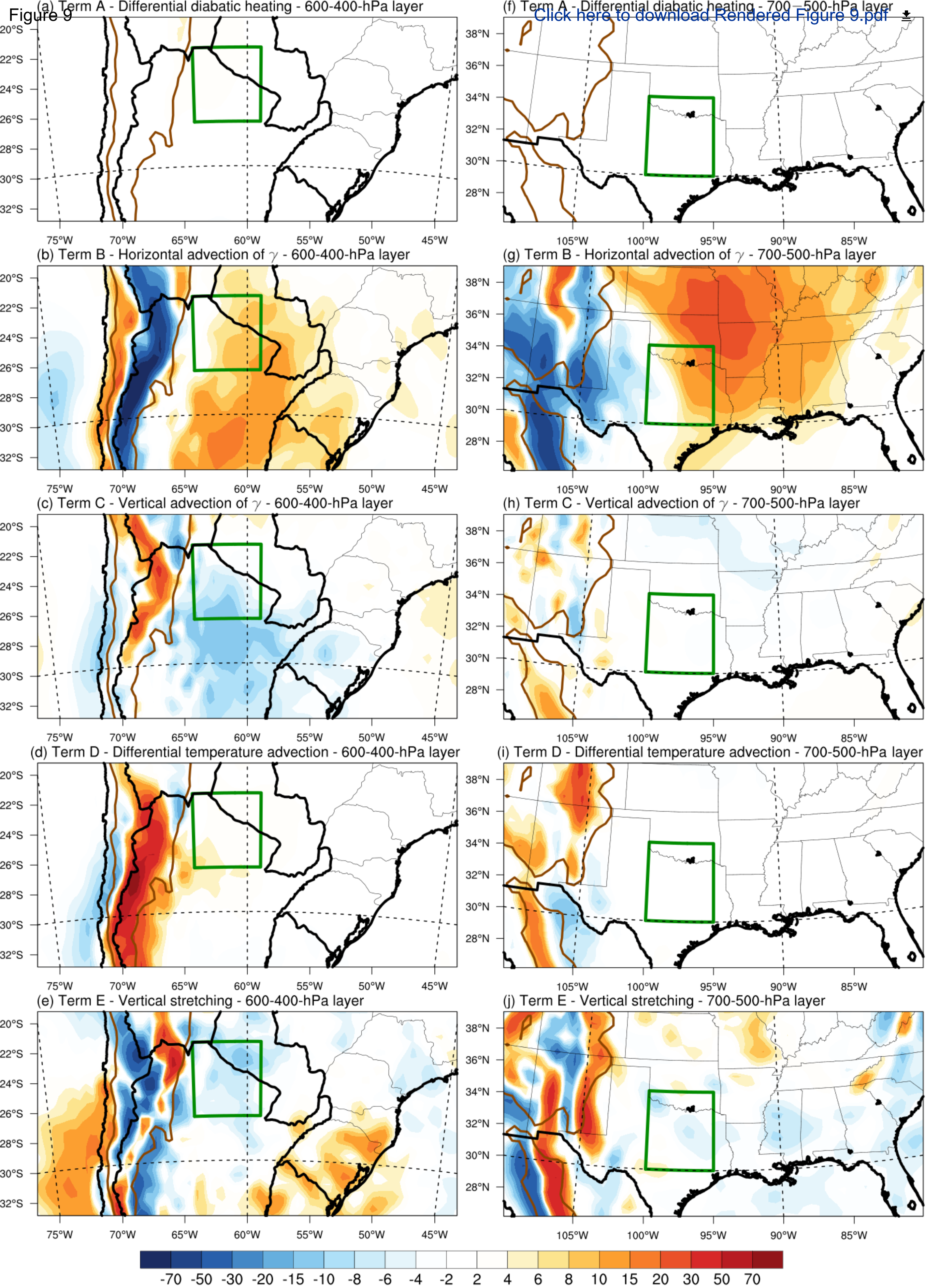

FIG. 9. γ tendency equation (a) term A, (b) term B, (c) term C, (d) term D, (e) term E in SA and (f) term A, (g) term B, (h) term C, (i) term D, (j) term E in NA (10^{-9} K m^{-1} s^{-1}, shaded). The terms are calculated from the composite fields of EML cases over R1 of each continent (gray squares) during spring, and are averaged over the 600–400-hPa layer in SA and 700–500-hPa layer in NA. The brown contour shows the 1500-m orographic contour.

FIG. 10. (a) Cross section from 90ºS to 90ºN along 85ºW of zonal wind magnitude (m s^{-1}, shaded), Ψ_M[10^{11} kg s^{-1}, negative values (anticlockwise circulation) in blue contours every –2 x 10^{11} kg s^{-1} starting at –1 x 10^{11} kg s^{-1}, and positive values (clockwise circulation) in red contours every 2 x 10^{11} kg s^{-1} starting at 1 x 10^{11} kg s^{-1}] and θ (K, grey contours every 10 K). (b) Cross section of zonal wind magnitude (m s^{-1}, shaded), θ (K, grey contours every 10 K), Ψ_M (10^{11} kg s^{-1}, negative values in blue contours every –2 x 10^{11} kg s^{-1} starting at –1 x 10^{11} kg s^{-1}, and positive values in red contours every 2 x 10^{11} kg s^{-1} starting at 1 x 10^{11} kg s^{-1}), and meridional ageostrophic wind (m s^{-1}, vectors) along the AA' line (68ºW) in Fig.1a. (c) Cross section of meridional ageostrophic wind with negative (positive) values denoting northerly (southerly) flow (m s^{-1}, shaded), θ (K, grey contours every 5 K), ω [10^{-2} Pa s^{-1}, negative values (ascent) in blue contours every –10 x 10^{-2} Pa s^{-1}, positive values (subsidence) in red contours every 10 x 10^{-2} Pa s^{-1}] along the BB' line (28ºS) in Fig. 1a.

Figure 11

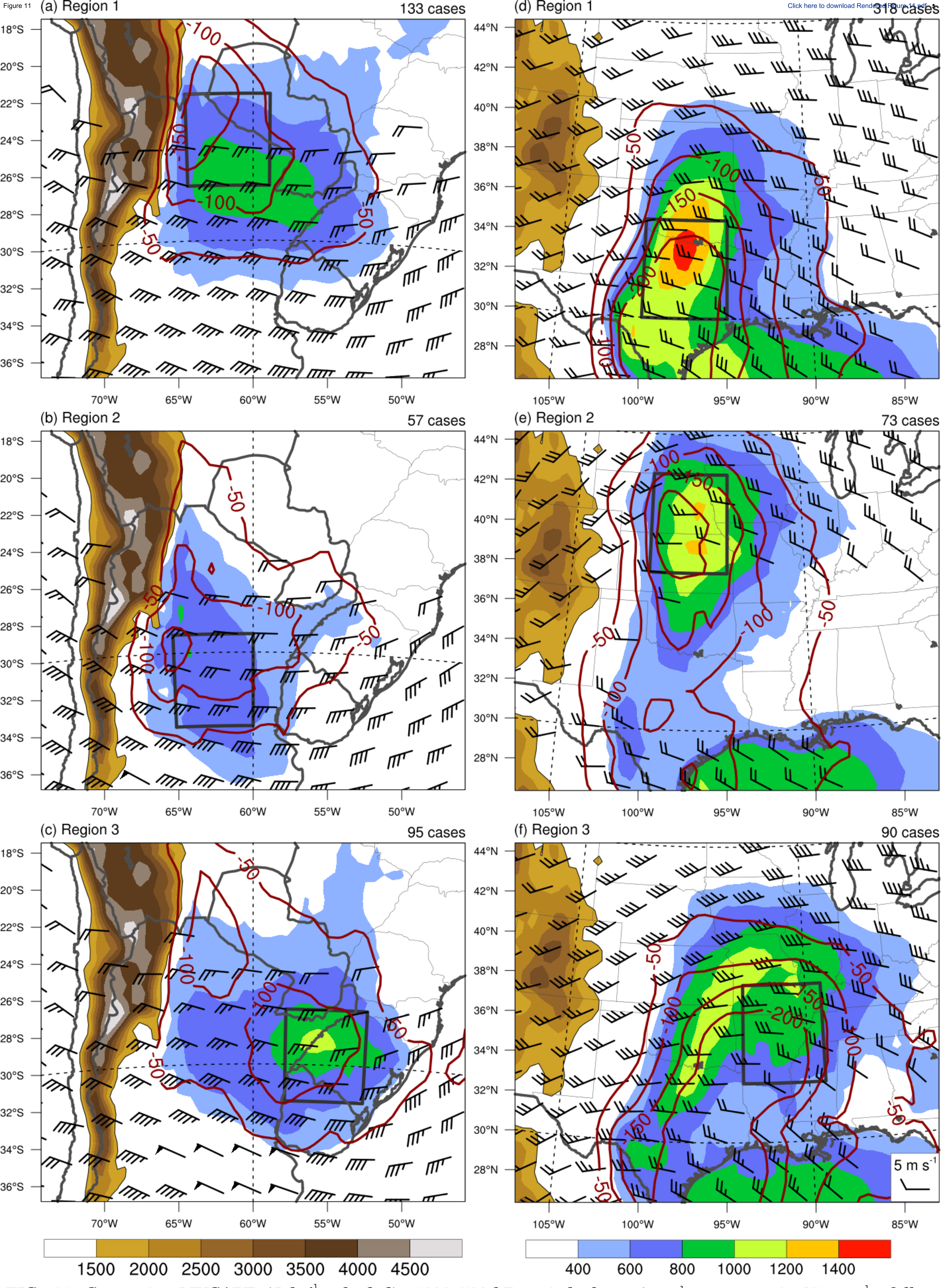

FIG. 11. Composite MUCAPE (J kg^{-1}, shaded), 1000–500-hPa wind shear (m s^{-1}, pennant is 25 m s^{-1}, full barb is 5 m s^{-1}, and half barb is 2.5 m s^{-1}; only wind barbs greater than 10 m s^{-1} are plotted), and CIN (J kg^{-1}, dark red contours every -50 J kg^{-1} starting in -50 J kg^{-1}) for EML cases in spring in (a) R1, (b) R2 and (c) R3 of SA and (d) R1, (e) R2 and (f) R3 of NA. Orography is shaded every 500 m starting in 1500 m. The 5º×5º areas are drawn in grey squares.

Figure 12

Click here to download Rendered Figure 12.pdf

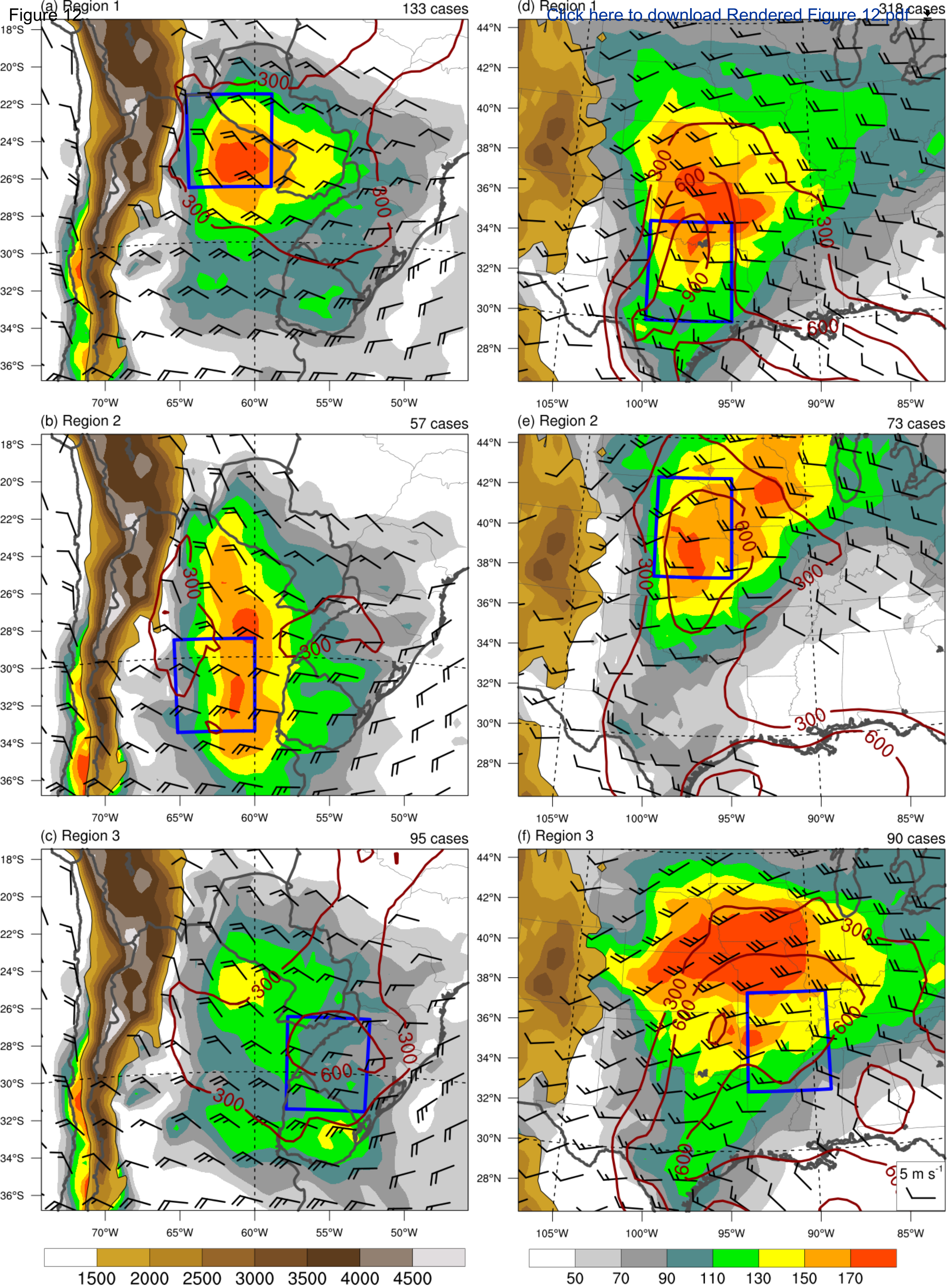

FIG. 12. Composite 0–3-km SRH magnitude (m² s⁻², shaded), 1000–700-hPa wind shear (m s⁻¹, pennant is 25 m s⁻¹, full barb is 5 m s⁻¹, and half barb is 2.5 m s⁻¹; only wind barbs greater than 5 m s⁻¹ are plotted), and SBCAPE (J kg⁻¹, red contours every 300 J kg⁻¹ starting in 300 J kg⁻¹) for EML cases in spring in (a) R1, (b) R2 and (c) R3 of SA and (d) R1, (e) R2 and (f) R3 of NA. Orography is shaded every 500 m starting in 1500 m. The 5°x5° areas are drawn in blue squares.

Figure 13

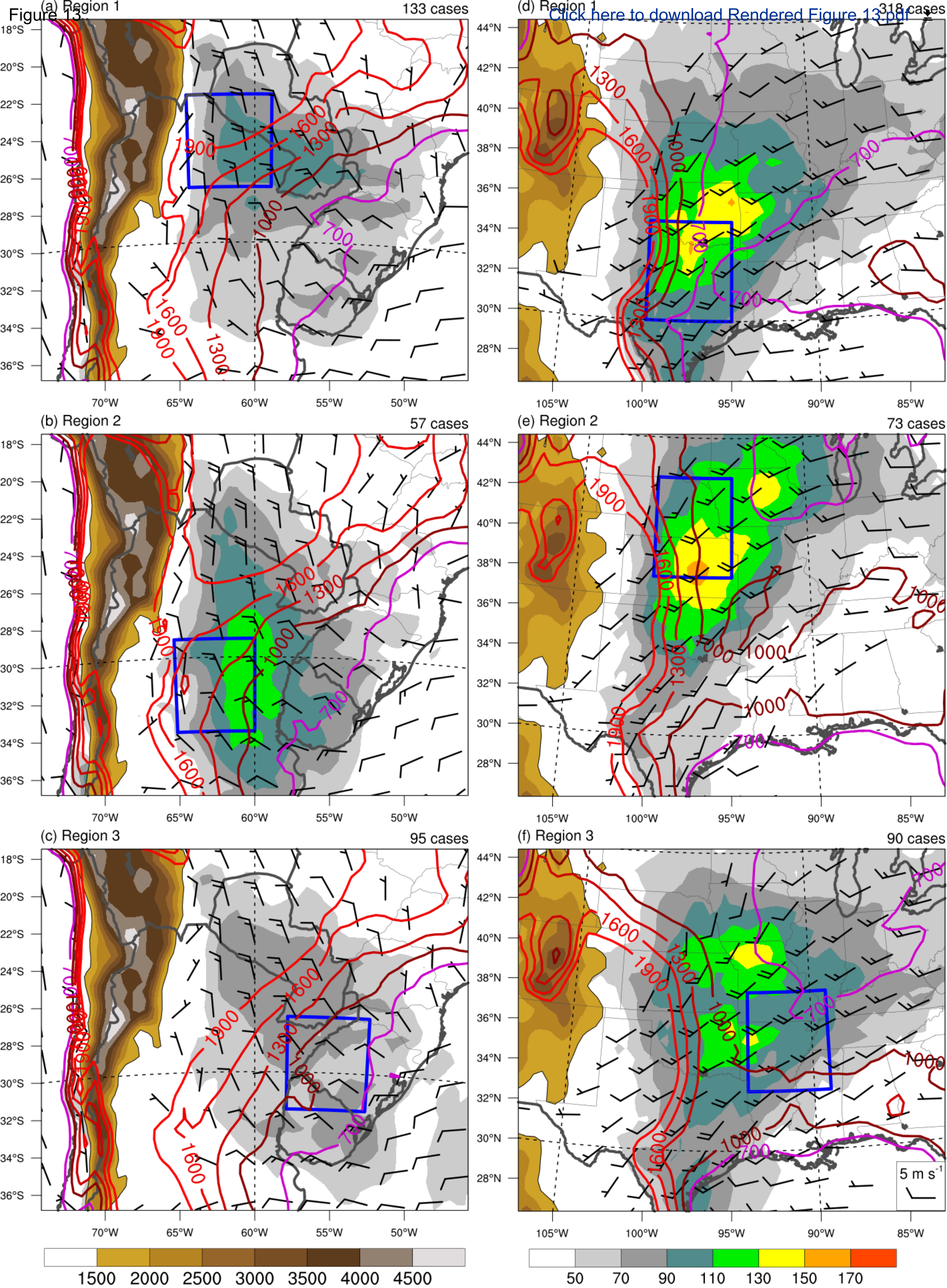

FIG. 13. Composite 0–1-km SRH magnitude (m² s⁻², shaded), 1000–850-hPa wind shear (m s⁻¹, pennant is 25 m s⁻¹, full barb is 5 m s⁻¹, and half barb is 2.5 m s⁻¹; only wind barbs greater than 2.5 m s⁻¹ are plotted), and LCL height (m, colored contours every 300 m starting at 700 m) for EML cases in spring in (a) R1, (b) R2 and (c) R3 of SA and (d) R1, (e) R2 and (f) R3 of NA. Orography is shaded every 500 m starting in 1500 m. The 5°x5° areas are drawn in blue squares.

Figure 14

Click here to download Rendered Figure 14.pdf

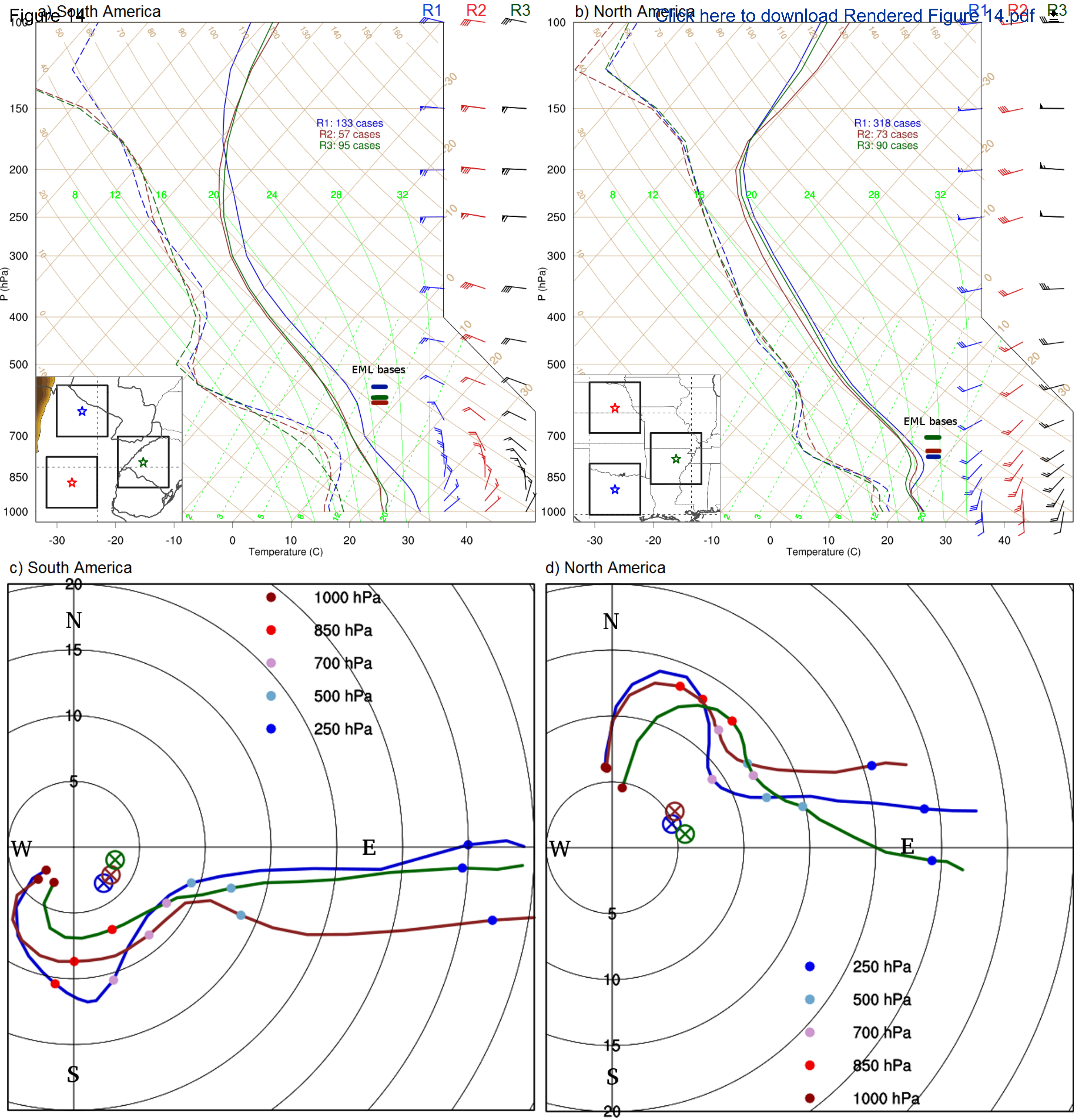

FIG. 14. Composite soundings and hodographs for R1 (blue lines), R2 (red lines) and R3 (green lines) of (a, b) SA and (c, d) NA in spring. The colored stars in the maps are the locations of the soundings and hodographs in the middle of the 5°x5° areas. EML bases are indicated by colored dashes for each sounding. In the hodographs, storm motion is represented by the operator symbols with the same colors, circles of same wind speed are shown every 5 m s^{-1}, and the dark red, red, magenta, light blue and blue dots mark the 1000, 850, 700, 500 and 250-hPa levels, respectively.

Figure 15

Click here to download Rendered Figure 15.pdf

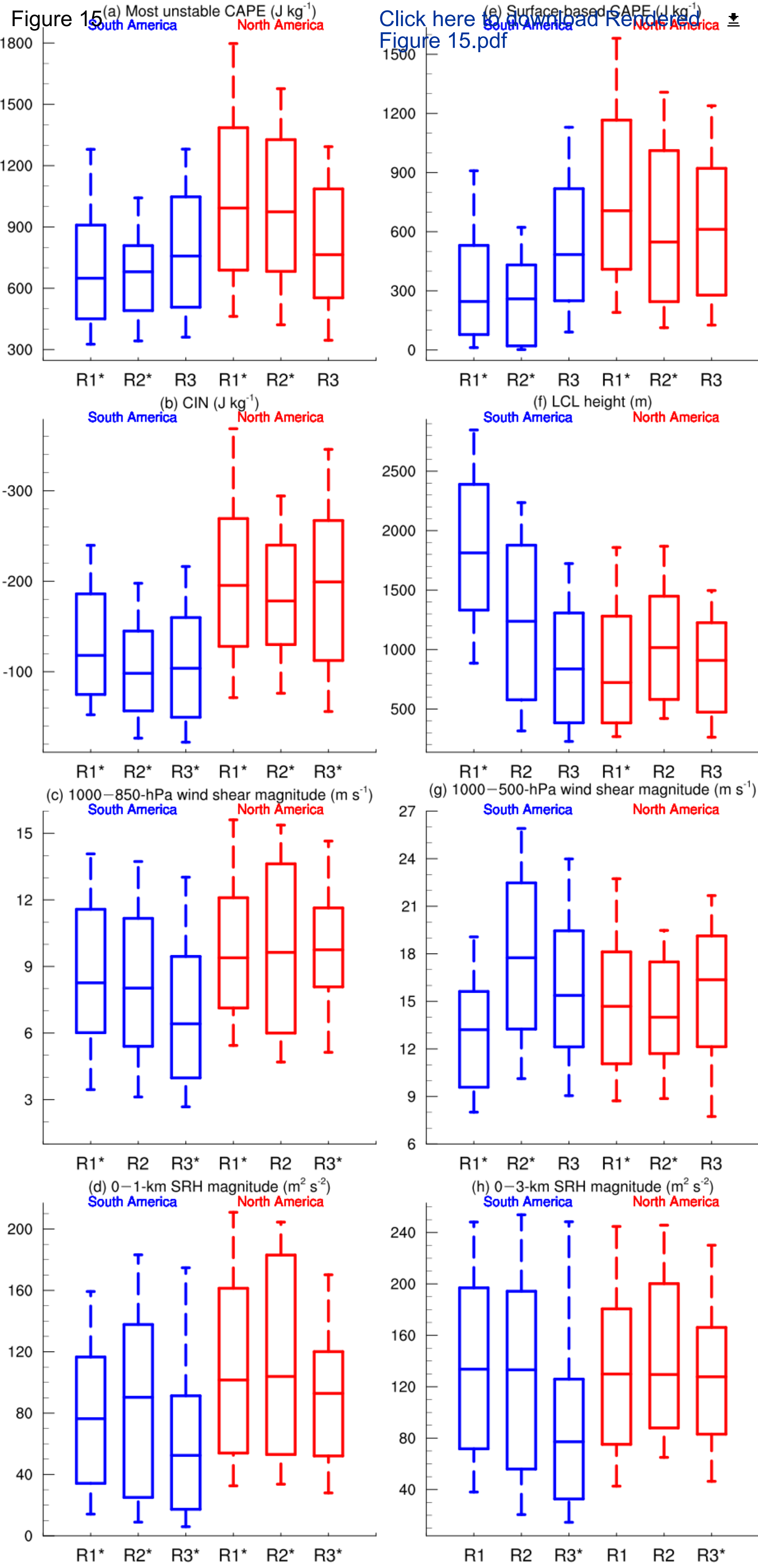

FIG. 15. Boxplots of the distributions of (a) MUCAPE (J kg^{-1}), (b) CIN (J kg^{-1}), (c) 1000–850-hPa wind shear magnitude (m s^{-1}), (d) 0–1-km SRH magnitude (m^2 s^{-2}), (e) SBCAPE (J kg^{-1}), (f) LCL height (m), (g) 1000–500-hPa wind shear magnitude (m s^{-1}) and (h) 0–3-km SRH magnitude (m^2 s^{-2}) over the R1–R3 regions of SA (blue boxplots) and NA (red boxplots) in EML cases during spring. Statistical parameters in the boxplot are the 90th and 10th percentiles (upper and lower tickmarks, respectively), 75th and 25th percentiles (upper and lower boxes boundaries, respectively) and median (line inside the boxes). Parameters that present statistically significant (95% confidence) differences between the same regions in the continents are marked with an astherisk (*) in the x axis. Details about the construction of the boxplots are found in the text.